SlimVar: rapid *in vivo* single-molecule tracking of chromatin regulators in plants

Alex L. Payne-Dwyer[1], Geng-Jen Jang[2], Caroline Dean[2], and Mark C. Leake[1,3]*

[1] School of Physics, Engineering and Technology, University of York, YO10 5DD, UK.

[2] Cell and Developmental Biology, John Innes Centre, Norwich Research Park, NR4 7UH, UK.

[3] Department of Biology, University of York, YO10 5DD, UK.

*Correspondence: mark.leake@york.ac.uk

Abstract

Epigenetic regulation maintains gene expression patterns over many rounds of cell division in higher organisms. However, visualization of factors regulating epigenetic switches *in vivo* is limited by the challenge of imaging cells deep in living tissue, with molecular sensitivity and rapid sampling. We report an easy-to-implement method called Variable-angle Slimfield microscopy (SlimVar), which by simple modification of an inverted optical microscope, enables single-molecule tracking of fluorescent reporters in *Arabidopsis thaliana*. Using SlimVar, we imaged stepwise photobleaching of chromatin-protein assemblies in individual nuclei, 30 µm deep in root tips through multiple cell layers. We find that two homologous proteins key to the epigenetic switch at *FLOWERING LOCUS C* (*FLC*) —cold-induced VERNALIZATION INSENSITIVE3 (VIN3) and constitutively expressed VERNALIZATION 5 (VRN5)—exhibit dynamic nuclear assemblies during *FLC* silencing. Upon cold exposure, these assemblies increase in stoichiometry by up to 100% to a median of ~20 molecules. Larger VRN5 assemblies preferentially co-localize with an *FLC lacO* transgenic reporter during prolonged cold, persisting after return to warm conditions. Our findings support a hybrid model of epigenetic memory in which nucleation of histone trimethylation is assisted by dynamic protein assemblies over extended durations. SlimVar therefore has potential to offer molecular insights into proteins expressed at physiological levels in a range of tissues.

Introduction

Understanding the mechanistic basis of epigenetic silencing remains a major question, with implications for cell differentiation and ageing through to crop security [1]. A conserved epigenetic mechanism across eukaryotes is Polycomb-mediated silencing [2], which involves the histone modification trimethylated histone H3 lysine 27 (H3K27me3). H3K27me3 initially accumulates at a nucleation site and then spreads across a locus to stably maintain a silenced state through many rounds of cell division [3], [4]. A gene where Polycomb Repressive Complex 2 (PRC2) silencing has been well studied is Arabidopsis *FLOWERING LOCUS C* (*FLC*) [5]. *FLC* encodes a repressor of flowering and is epigenetically silenced during a process called vernalization by the prolonged cold of winter; repression of a repressor thus enables flowering in spring [6], [7], [8]. Cold exposure increases the proportion of *FLC* alleles that have epigenetically switched from ON to OFF states through nucleation of H3K27me3 at an intragenic site [9], [10]. Upon return to warm conditions, H3K27me3 spreads across the locus to give long-term stable silencing [11]. The relative stability of the nucleated state

through cell division in the cold at *FLC* has raised an interesting question as to the mechanism of epigenetic inheritance. Each nucleation event involves only three nucleosomes, too few to survive random replicative dilution through the classic Polycomb 'read-write' mechanism [8], [12], [13]. Metastable protein assemblies have been proposed to explain the inheritance of the nucleated state [14]. PRC2 accessory proteins are thought to restore the stochastic loss of histone marks by stimulating Polycomb Repressive Complex 2 (PRC2) activity [15]. While individual proteins may only interact transiently with nucleation factors and the locus, an assembly (with the appropriate positive cooperativity) is predicted to become dynamically self-sustaining above a threshold number of recruited proteins [14]. In this framework, a sufficiently large assembly could therefore act as a binary memory element working together with established H3K27me3 machinery at a given locus.

Two PRC2 accessory proteins required for stable cold-induced silencing at *FLC*, VERNALIZATION INSENSITIVE3 (VIN3) and VERNALIZATION 5 (VRN5, also known as VIN3-LIKE 1 / VIL1), expressed in shoot and root tips are clear candidates for this form of memory storage [16]. VIN3 and VRN5 (collectively called VEL proteins) associate with the PRC2 complex and with the *FLC* nucleation region that accumulates H3K27me3 specifically during cold conditions [8], [17]. At <15°C, *VIN3* expression gradually rises over several weeks, while in warm conditions >15°C, expression decays rapidly within ~4h [6], [7], [17]. VIN3 and its assemblies could therefore in principle report the duration of cold conditions during winter to promote an epigenetic switch. However, due to its instability in the warm, one or more additional factors—a promising candidate being VRN5—are required at the *FLC* nucleation region to explain persistent memory of silencing following a change to warm conditions. Both VIN3 and VRN5 contain complex plant homeodomains (PHDs) [16] which do not interact directly with histone tails [20], FNIII domains and C-terminal VEL domains [18], [19]. Of these three domains common to VIN3 and VRN5, the VEL domain mediates head-to-tail interactions. VEL proteins that oligomerize and even form phase-separated droplets under transient overexpression are directly associated with stable silencing at *FLC* [19]. A key question is then: do physiological levels of VIN3 and VRN5 oligomerize sufficiently in the vicinity of *FLC* during vernalization, to fulfil this model?

Here, we describe development of an efficient new imaging modality, Slimfield Variable Angle (SlimVar) and apply it to rapidly track VEL proteins in live plant tissue. Investigation of nuclear oligomers has been constrained by an inability to detect individual, rapidly diffusing protein molecules deep within plant tissue. Traditional confocal [21], structured illumination [22] and lightsheet [23] methods lack the required combination of sensitivity and speed for single-molecule tracking in live plants, which remains a technical challenge beyond the first cell membrane [24], [25], [26], [27], [28], [29], [30], [31]. Although complex and expensive super-resolution methods including lattice lightsheet [32], [33] and MINFLUX [34], [35] are capable of deeper imaging, to date none have been adequately optimised in plants. In addition, these typically require both specialised hardware and photoactivatable / photoswitchable fluorescent proteins [36], [37] or dyes [38], [39]. Our method, SlimVar, instead leverages common fluorophore fusions in existing transgenic plants, and an accessible microscope platform. SlimVar adapts Slimfield microscopy [40], [41], [42] with a grazing angle of incidence optimal for observing single nuclei up to ~30 µm deep in root tissue, while tracking single fluorescent protein molecules at 40 nm resolution. Whereas

normal Slimfield has been limited to simple unicellular samples or the surfaces of *ex vivo* tissue sections [43], SlimVar enhances the image contrast to enable dynamic spatial localization in complex multicellular samples. The use of root tips confers optical advantages of lower autofluorescence and more regular, less refractive layers than other plant tissues. This single-molecule sensitivity can be combined with stepwise photobleaching analysis [40] to quantify the number of molecules in any observed oligomeric assemblies. This sensitivity simplifies use of transgenic plant lines expressing from as few as a single gene copy and enables imaging of physiological states of low-abundance nuclear proteins.

We find that both VIN3 and VRN5 proteins form assemblies in cell nuclei, composed of consistent dimeric subunits. In lines expressing from single-digit exogenous copies of VIN3 and VRN5, the median assembly comprises up to ~20 molecules of each protein, in agreement with the required stoichiometry of protein memory elements predicted from modelling [14]. We also use an *FLC-lacO*/LacI-YFP transgenic reporter to localize the *FLC* locus and characterise its mobility relative to VEL proteins. Finally, we demonstrate dual-colour SlimVar, which directly shows VRN5 assemblies present at *FLC*. We find that larger VRN5 assemblies preferentially colocalize with *FLC* after long cold exposure and after return to warm conditions, and that this interaction between individual larger oligomers of VRN5 and *FLC* is dynamic on a sub-second timescale.

Results

SlimVar resolves dynamic single particles of VIN3 and VRN5 in plant nuclei

As an initial benchmark, we used traditional confocal imaging with a typical sampling time of 35 s per frame to examine VIN3 and VRN5 protein localization, during and after cold treatment (Fig. 1b, Col*FRI* negative control Supplementary Fig. 1). We utilised lines with VRN5-EYFP*/vrn5-8 JU223* [8], [16] or VIN3-EGFP/*vin3-4 FRI* [8], [44] (referred to as VRN5-YFP and VIN3-GFP respectively). To investigate the effects of protein expression and to exploit the greater imaging contrast and lower autofluorescence associated with yellow and red fluorophores, we later also characterised new VIN3-SYFP2/Col*FRI* line (Supplementary Figs. 2 and 3) and VRN5-mScarlet-I/*vrn5-8 FRI* lines (Supplementary Fig. 4). These lines include active *FRI* alleles so require effective vernalization for flowering [17]. After identifying nuclei from transmitted light images, we found that both VIN3 and VRN5 exhibited high intensity but largely diffuse fluorescence localized to the nucleoplasm. While VRN5 was detectable well above background levels in all nuclei (N=241) at all timepoints, VIN3 was only discernible at diurnal maxima during the cold period itself. Its level decreased at subsequent timepoint after this, being undetectable within one week after return to warm conditions, as reported previously [7]. During cold, the VIN3 signal per cell was initially greatest in the vicinity of the meristem and epidermis, before becoming brighter in all cells after further cold exposure. We then optimised Airyscan, an enhanced form of confocal laser scanning microscopy which uses a point detector array to obtain faster frame sampling times down to 60 ms for individual root tip nuclei [45]. Images showed a marginally more granular spatial patterning for VIN3 and VRN5 than standard confocal, hinting at the presence of distinct foci within the diffusive fluorescence (Fig. 1c).

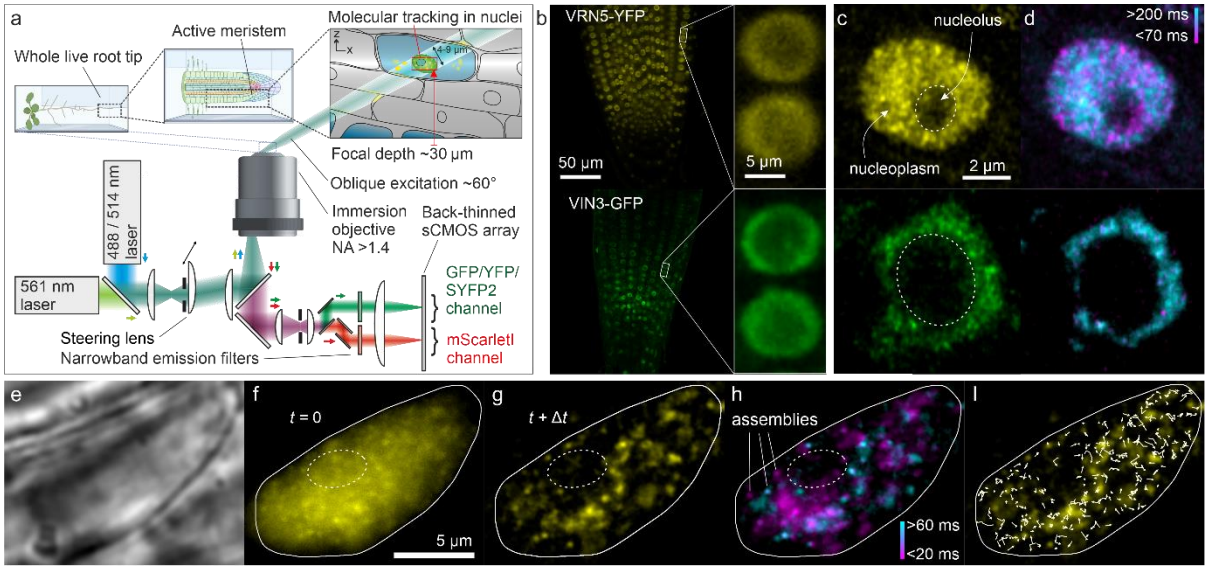

Figure 1. SlimVar resolves single particle dynamics of VIN3 and VRN5 during cold exposure of root tips. a) The optical scheme for single- or dual-colour excitation with beam delivery at a steep angle into a live root sitting on an agarose pad. The intersection of the focal plane and the excitation beam defines a thin detection volume, closely matched to the nuclear dimensions up to 30 µm deep into live tissue. High numerical aperture, high laser intensity and a photon-efficient sensor all contribute to the speed and sensitivity required to detect single molecule dynamics. b) Projections of confocal z-stacks of live whole root tips of VIN3-GFP and VRN5-YFP after 6 weeks of cold; insets (interpolated) show detail of the labelled protein signals, which are consistently localized to the nucleoplasm, but not the nucleolus. The nuclear patterning of VIN3 and VRN5 was typically either round or lens-shaped depending on cell type and cell wall attachment, with a median length 7.8 µm (interquartile range IQR: 5.7–10.3 µm, N=571), and median aspect ratio of 1.16 (IQR: 1.06–2.10), comparable to other nuclear reporters [46]. Acquisition time is 35s. c,d) Airyscan images of VRN5-YFP and VIN3-GFP after 2 weeks' cold indicating heterogeneity spatial distribution; c) maximum intensity projection of three *z*-slices, averaged over three consecutive timepoints; d) sensitivity to the dynamics over the same three timepoints represented by contrast between median (cyan) and standard deviation (magenta) of the pixel values over time, the latter indicating faster detected motion of VRN5 compared to VIN3 assemblies. e-h) SlimVar microscopy of VRN5-YFP before vernalization; e) brightfield, f) initial frame in YFP channel prior to photobleaching; g) early stage photobleaching revealing distinct assemblies (mean projection of frames 4–6); h) SlimVar resolves assemblies of differential mobility on 20 ms timescales shown here as distinct slow- (cyan) and fast-moving (magenta) objects, represented by median and standard deviation projections over three frames. i) Automated tracking analysis (Methods) identifies assemblies to super-resolved localization precision and estimates the corresponding stoichiometry and mobility. Individual tracks are shown as arrows with one vertex per timepoint.

We then implemented SlimVar (Fig. 1a), capable of single-molecule fluorescent protein detection at sub-ms levels, and found the same nucleoplasmic localization, but instead of diffuse fluorescence we observed multiple individual distinct fluorescent foci (Fig. 1d) consistent with a greater sensitivity and sampling speed that eradicates motion blur from

mobile protein assemblies. SlimVar employs a very narrow field of oblique-angle epifluorescence illumination (similar to variable angle epifluorescence microscopy (VAEM) [47] and highly inclined illumination (HILO) [48], [49]) and high localized excitation intensities to enable millisecond sampling. To achieve this, the excitation laser is focused into the back focal plane of a high numerical aperture immersion objective lens at a precise lateral displacement from the optic axis. To mitigate refractive index mismatch and facilitate deeper tissue imaging up to 30 µm from the coverslip surface, we performed optimisation at a representative depth of 20 µm in a live root sample (Methods). The resulting beam is sufficient to encapsulate individual cell nuclei between 4–16 µm wide but with minimal excitation of the remaining >70% of the cell volume. It is ideally aligned for the target root tip cells in the epidermis, cortex and endodermis overlaying the stem cell niche (Fig. 1a), with associated reduction in aberration, backscatter and out-of-focus fluorescence excitation of intermediate cell layers, including the lateral root cap. The net result is an improvement in signal-to-noise for imaging VIN3 and VRN5 fluorescent reporters by a factor of ~3 (Methods), enabling independent single-molecule detection consistent with control samples of purified fluorescent protein (Supplementary Fig. 5).

Vernalization induces upregulation and self-assembly of VIN3 and VRN5

We integrated the pixel intensities in SlimVar images to quantitatively determine the nuclear abundance of VIN3 and VRN5 (Methods). The counts per nucleus were normalised by the characteristic intensity due to a single fluorescent protein, determined by single-molecule photobleaching steps *in situ* [40] (Supplementary Fig. 5). We define the nuclear protein copy number as the difference in mean integrated intensity (Fig. 2) between the test population and the negative control, Col*FRI*, and identify this with the total number of labelled molecules of either VIN3 or VRN5 in a typical nucleus.

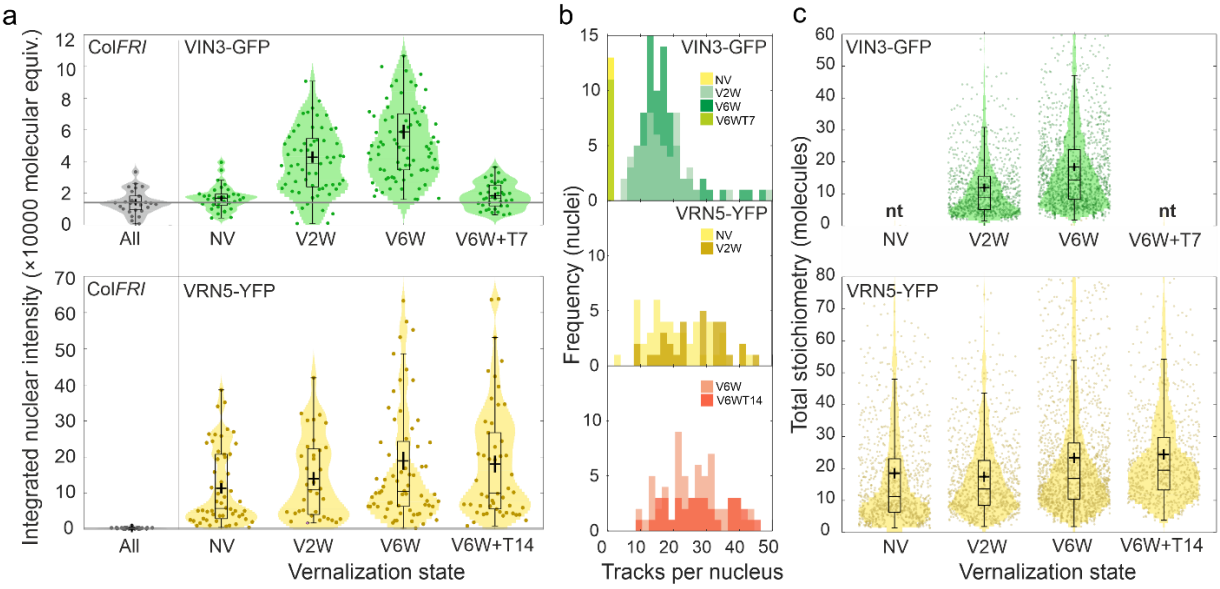

Figure 2. Cold exposure causes VIN3 and VRN5 to form assemblies each of larger, more broadly distributed stoichiometry, and a relatively modest increase in the number of assemblies. a) Distributions of integrated nuclear intensity (total number of labelled molecules per nucleus prior to correcting for autofluorescence) of individual nuclei aggregated across cell type at different timepoints before, during and after vernalization, for exogeneous VIN3-GFP and VRN5-YFP. The nuclear protein copy number (number of labelled molecules excluding any associated with autofluorescence) is then calculated as the net excess above the mean level of the negative control Col*FRI* (horizontal line), which represents autofluorescence background. Bar, box and whisker denote median, interquartile range (IQR) and 1.5× IQR respectively; cross: mean ± sem. The abundance of VIN3 protein was insignificant prior to vernalization (Brunner-Munzel (BM) test vs Col*FRI*, N=66, p=0.11 |ns: not significant at adjusted p<0.01). However, the VIN3 nuclear protein copy number increases sharply to ~28,000 ± 3,700 molecules above control after 2 weeks cold (N=64, p=0.0031 |*), and peaks at ~44,000 ± 4,700 after 6 weeks cold (N=83, p<0.001 |**). Following transfer to warm conditions, VIN3-GFP levels reduce to ~3,200 ± 1,600 molecules within 7 days (N=74, p=0.04 |ns). VRN5 levels increase between non-vernalized and post-vernalized timepoints from ~110,000 ± 23,000 to ~190,000 ± 37,000 molecules (N=94, p=0.0089|*). b) Distributions of the number of tracks per nucleus (binned in columns of width 2 for clarity). The number of VRN5 tracks increases initially (NV: 20.8 ± 1.9 up to 26.8 ± 1.6 tracks per nucleus at 2 weeks cold; N=86, p=0.0054|*) but stops increasing after 6 weeks' cold (27.0 ± 1.5 and 26.2 ± 2.6 tracks per nucleus at 6 weeks cold and 14 days post-cold respectively; N=94, p=0.80|ns); c) Collated distributions of stoichiometry (number of labelled molecules per nuclear assembly) of individual tracks at different timepoints before, during and after vernalization; *nt*: no tracks detected.

We explored the effect of transgene copy number on the abundance of the VEL proteins. We generated a homozygous single transgene copy line of VIN3-SYFP2, though not in a deletion background, meaning endogenous VIN3 is also present at a similar level (Supplementary Fig 2a.). The expression of exogenous VIN3 still follows the expected pattern (Supplementary Fig 1.) but at much lower levels, reflecting the reduction to a single transgene copy of *VIN3*. In both VIN3 fusions the nuclear protein copy number exhibits an increase from two to six weeks (Fig 2a., Supplementary Fig 3a.), although the distributions partially overlap. The two-week level is between half and two-thirds of the six-week level that approaches full vernalization. VRN5 was highly abundant at all timepoints, with levels an order of magnitude greater than VIN3 in the VIN3-labelled lines (Fig 2a). The total amount of VRN5 approximately doubles in response to full vernalization and persists after return to warm conditions. Nuclear protein copy numbers translate to nucleoplasmic concentrations of ~100 nM–1 µM for VIN3 and 1–10 µM for VRN5 (Methods). When applied to the cell cytoplasm, the high sensitivity of SlimVar was also able to establish an upper bound to the fluorescent signal for both VIN3 and VRN5 marginally above the Col*FRI* negative control levels, equivalent to a concentration approximately four orders of magnitude smaller than those measured in the nucleus.

Using SlimVar, highly motile fluorescent foci for both VIN3 and VRN5 could be tracked for up to ~20 consecutive image frames before photobleaching of nuclear contents occurred (Supplementary Videos 1, 2). Using bespoke tracking software (Methods) we found that these nucleoplasm-localized protein assemblies were largely excluded from the nucleolus, evident as dark regions of effective diameter 3–6 µm (Fig. 1c). In larger nuclei, the centres of nucleoli also appeared to exhibit weak VIN3 and VRN5 localization (Fig. 1b,c). We detected 10-40 tracks per nucleus while no tracks were detected either in the negative control or for VIN3 at pre- or post-vernalized timepoints (Fig. 2b). The number density of VRN5 tracks increased by about a third over the vernalization time course (0.55 ± 0.05 and 0.71 ± 0.05 μm^{-2} before cold and 14 days post-cold respectively: N=62, p=0.0042|*). Specifically, the mean number of VRN5 tracks per nucleus increased after the onset of vernalization and this increase was maintained after return to warm (Fig. 2b). We characterised the average characteristic brightness of a single molecule of the corresponding fluorescent protein (Methods) to determine the bleach-corrected stoichiometry of each track, with which we identified the number of labelled VIN3 or VRN5 molecules in each detected assembly. We found that both VIN3 and VRN5 exhibited broad stoichiometry distributions from a few molecules up to several tens of molecules for individual assemblies (Fig. 2c) and that the average stoichiometry increased with time duration spent in the cold during vernalization. For VIN3, the mean stoichiometry was 12.0 ± 0.4 molecules at V2W, increasing to 18.6 ± 0.5 molecules at V6W (N=1,988, p<0.001|**). For VRN5, assemblies were found to be well developed prior to vernalization (mean 18.5 ± 0.6 molecules at NV). However, there was an increase in stoichiometry during vernalization which persisted after the return to warm conditions (mean of 24.4 ± 0.9 molecules at V6W+T14; N=1,626, p<0.001|**). The greatest change occurred during the intermediate stages of vernalization between V2W and V6W (17.4 ± 0.7 to 23.4 ± 0.6 molecules, N=1,928, p<0.001|**). About ~1% of the nuclear protein copy number was detected in tracks at the fixed focal z-position, which compares well with our estimate, based on the theoretical depth-of-field, that ~4% of the mean nuclear volume is in sharp focus in each frame.

Multimolecular assemblies of VIN3 and VRN5 contain multiples of two molecules

The stoichiometry distributions each show a series of periodic peaks (Fig. 3) that are revealed when represented as a kernel density estimate, a method which objectifies the equivalent histogram bin width used. If the assemblies represented have a common oligomeric structure, the characteristic peak spacing is then equivalent to the number of molecules associated with a physical subunit of the assembly [50]. We developed a new analysis method to discriminate this periodicity using the most common nearest-neighbour peak intervals. We verified it using realistic statistical simulations (Methods) and experimental data from standard LacI tetramers *in vivo* [51] (Supplementary Figs 6 and 7). Both VIN3 and VRN5 exhibit neighbouring peaks in their stoichiometry distributions which are separated by two molecules (Fig 3 insets). Performing identical SlimVar imaging on the VIN3-SYFP2 line indicated comparable levels of VIN3 nuclear protein copy number when corrected for the unlabelled VIN3 present using qPCR (Methods), but indicated stoichiometry values, and a characteristic peak spacing of stoichiometry, of approximately half that observed in the VIN3-GFP line (Supplementary Fig. 2), suggesting that the measured 2-molecule periodicity is unlikely to be an effect driven by dimerization of the fluorescent protein tag as reported in bacterial studies [52].

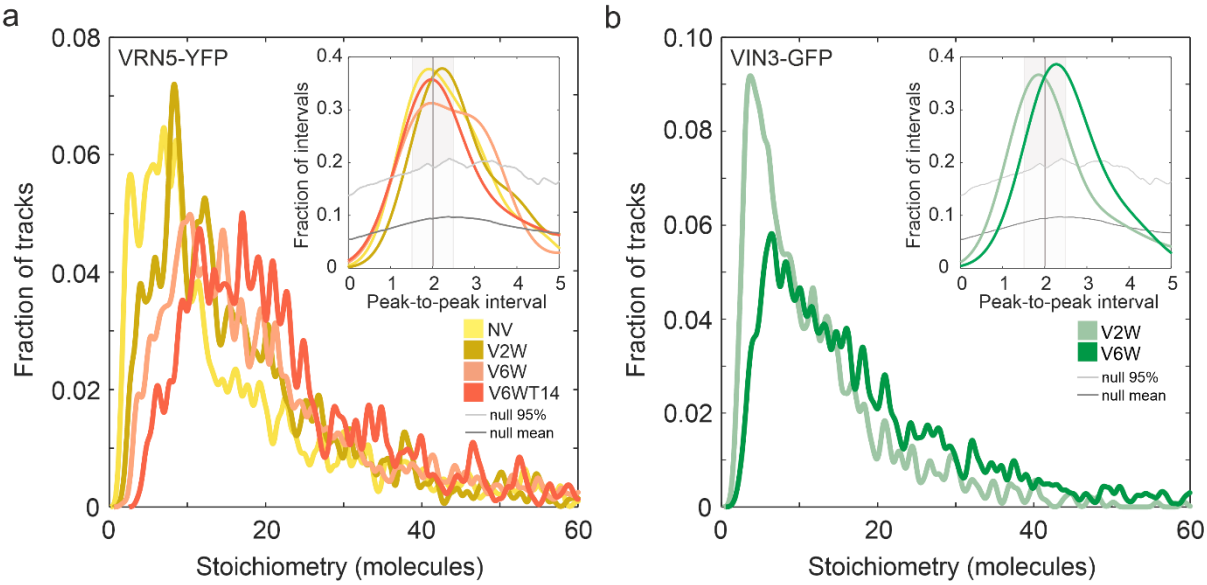

Figure 3. VIN3 and VRN5 assemblies exhibit a two-molecule spacing in their stoichiometry distributions. The number of labelled molecules in each assembly shows consistent periodicity of a) VRN5-YFP and b) VIN3-GFP. The fixed kernel width of 0.6 molecules corresponds to the rms error in the observation of a single molecule. Insets: the number of molecules in this subunit can be estimated from the most common spacing between neighbouring peaks in each stoichiometry distribution. The threshold above which a null (aperiodic) distribution can be rejected is the 95th percentile fraction of intervals (grey trace) output from simulated random stoichiometry (Methods). The most common interval is given by the modal kernel density estimate ± sem above the null threshold (VIN3-GFP: V2W, 1.9 ± 0.3; V6W, 2.2 ± 0.3. VRN5-YFP: NV, 1.9 ± 0.4; V2W, 2.2 ± 0.4; V6W, 2.0 ± 0.3; V6W+T14, 2.0 ± 0.4). The periodic unit in each of these cases is consistent only with an assembly subunit of 2 molecules of either VIN3-GFP or VRN5-YFP.

Mobility of larger VIN3 and VRN5 assemblies matches that of *FLC* during cold exposure

We estimated the microscopic diffusion coefficient *D* for each detected track by calculating the gradient to the initial portion of its corresponding mean square displacement (see Methods). We found that VIN3 assemblies became significantly less mobile between two and six weeks of cold exposure (Fig. 4b, Supplementary Figure 3e). VRN5 assemblies exhibited a similar ~20% decrease in diffusivity during the same central stage of vernalization (Fig. 4c).

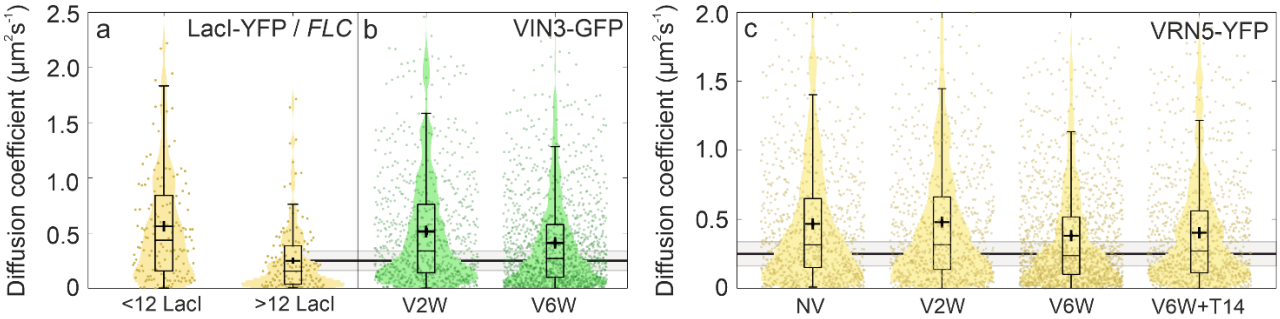

Figure 4. Microscopic diffusion coefficients of VIN3 and VRN5 assemblies decrease towards that of *FLC* loci during vernalization. a-d) The diffusion coefficients, *D*, of individual tracks as estimated from mean-square displacement analysis. a) LacI-YFP tracks of fewer than 12 molecules, detected from nuclei without pre-bleaching and identified as unbound LacI, and of LacI-YFP tracks of more than 12 molecules after pre-bleaching, identified as *FLC* candidates; b) Diffusion coefficients of VIN3-GFP and c) VRN5-YFP before, during and after vernalization. VIN3-GFP and each exhibit a decrease in mobility during the latter part of vernalization, persisting in VRN5 following return to warm conditions: (VIN3-GFP: D = 0.52 ± 0.03 to 0.41 ± 0.01 $\mu m^2 s^{-1}$; mean ± sem; N=672, p=0.0011|*; VIN3-SYFP2: D = 0.58 ± 0.02 to 0.49 ± 0.02 $\mu m^2 s^{-1}$; N=1,552, p<0.001|**; VRN5-YFP: 0.47 ± 0.02 / 0.48 ± 0.02 $\mu m^2 s^{-1}$ at NV / V2W to 0.38 ± 0.01 / 0.40 ± 0.02 $\mu m^2 s^{-1}$ at V6W / V6W+T14; N≥982, p=0.0072 |*). Horizontal lines denote diffusion coefficient of *FLC-lacO*/LacI-YFP foci under the same conditions (solid line: mean value; grey area, agreement within error).

For comparison with the diffusivity of *FLC* loci, we performed SlimVar imaging of a *FLC-lacO*/LacI-YFP line with 120 *lacO* copies integrated downstream of the *FLC* transgene [53]. To obtain a qualitative indication of the proportion of VIN3 and VRN5 assemblies which might be bound to *FLC* and their stoichiometry, we analysed just tracks whose diffusion coefficient was comparable to that of a typical *FLC* locus (D_{FLC} = 0.20 $\mu m^2 s^{-1}$, Supplementary Figure 6) within individual track measurement error (± 0.07 $\mu m^2 s^{-1}$) such that *D* lies in the range 0.13 – 0.27 $\mu m^2 s^{-1}$ (Fig. 4a). This simple method of diffusivity matching [54] is particularly helpful when only single-label lines are available. The subset of VIN3 or VRN5 assemblies with diffusivity consistent with *FLC* (Table 1) have stoichiometries distributed similarly to the full cohort of VIN3 or VRN5 tracks (Fig. 3c) and show similar increases in stoichiometry over the course of vernalization for both VIN3 and VRN5. The median stoichiometry of each protein using this diffusivity matching was in the range 10-20 molecules per assembly, increasing with vernalization.

Table 1. Average stoichiometry of VIN3-GFP and VRN5-YFP assemblies whose diffusivity matches that of *FLC* loci. The diffusivity-matched stoichiometry is distributed similarly to the population (VIN3-SYFP2 V6W, N=296, p=0.08 |ns), and similarly increases with vernalization for both VIN3 (V2W to V6W, SYFP2: N=262, p<0.001 |**; GFP: N=302, p<0.001 |**) and VRN5 (NV to V6W+T14, N=318, p<0.001 |**).

Line	**Timepoint**	***FLC*-like tracks** $D \approx D_{FLC}$		**Stoichiometry** (molecules)	
		Number	% of total (± sem)	Median	IQR
VIN3-GFP	V2W	151	15.2 (1.2)	9.9	5.9–16.3
	V6W	262	17.6 (1.1)	15.1	9.0–26.0
VRN5-YFP	NV	203	18.4 (1.3)	11.3	7.3–23.4
	V2W	168	17.4 (1.3)	17.7	11.1–29.9
	V6W	355	20.8 (1.1)	18.1	11.5–30.2
	V6W+T14	249	19.6 (1.2)	20.4	12.7–31.0

In keeping with the increase in stoichiometry and lower diffusivity, the proportion of VIN3 assemblies that show slow *FLC*-like diffusion increases from around 11-15% during early stages of vernalization up to around 17-18% (Table 1). The fraction of *FLC*-like VRN5 assemblies present in the nucleus is already ~18% prior to vernalization and maintains this level throughout. However, given the vastly greater concentration of VEL protein assemblies compared to *FLC* loci, this proportion is unlikely to be representative of VEL localizations at *FLC*, which if present, would be a minority observable only by direct colocalization.

VRN5 assemblies of greater stoichiometry are enriched at *FLC* during and after vernalization

To directly track VRN5 at the *FLC* locus, we generated transgenic plants co-expressing VRN5 (fused to mScarlet-I [55], mScI) and *FLC-lacO* (via LacI-YFP) for dual-colour SlimVar. Our test for colocalization of VRN5 at *FLC* first required a reliable method to identify *FLC* without perturbing the mScarlet-I reporter for VRN5. For each nucleus, we first performed a rapid z-stack using 514 nm laser excitation to screen for and localize bright, low mobility LacI-YFP foci consistent with *FLC* transgenes (Fig. 5a). At a chosen z-position containing one or more of these *FLC* candidates, we then tracked VRN5-mScI and LacI-YFP in a time course using alternating laser excitation (Methods); most images were dominated by the presence of unbound LacI-YFP foci, however, we measured a distinct subset bound to *FLC* (Fig. 5b) with a frequency of 2.3 ± 1.4 (mean ± sd) per nucleus in the meristem, matching the expectation of 2 *FLC* loci per nucleus within experimental error [53]. This rose to 3.3 ± 1.7 per nucleus in cells toward the transition zone, consistent with more nuclei exhibiting additional pairs of *FLC* loci under genomic endoreduplication. Approximately 40% of detected *FLC* loci were colocalized with VRN5-mScI assemblies, though this proportion was constant across all vernalization times. This led us to question: might a putative memory element be conditional on the properties of the colocalized VRN5 assemblies, such as stoichiometry?

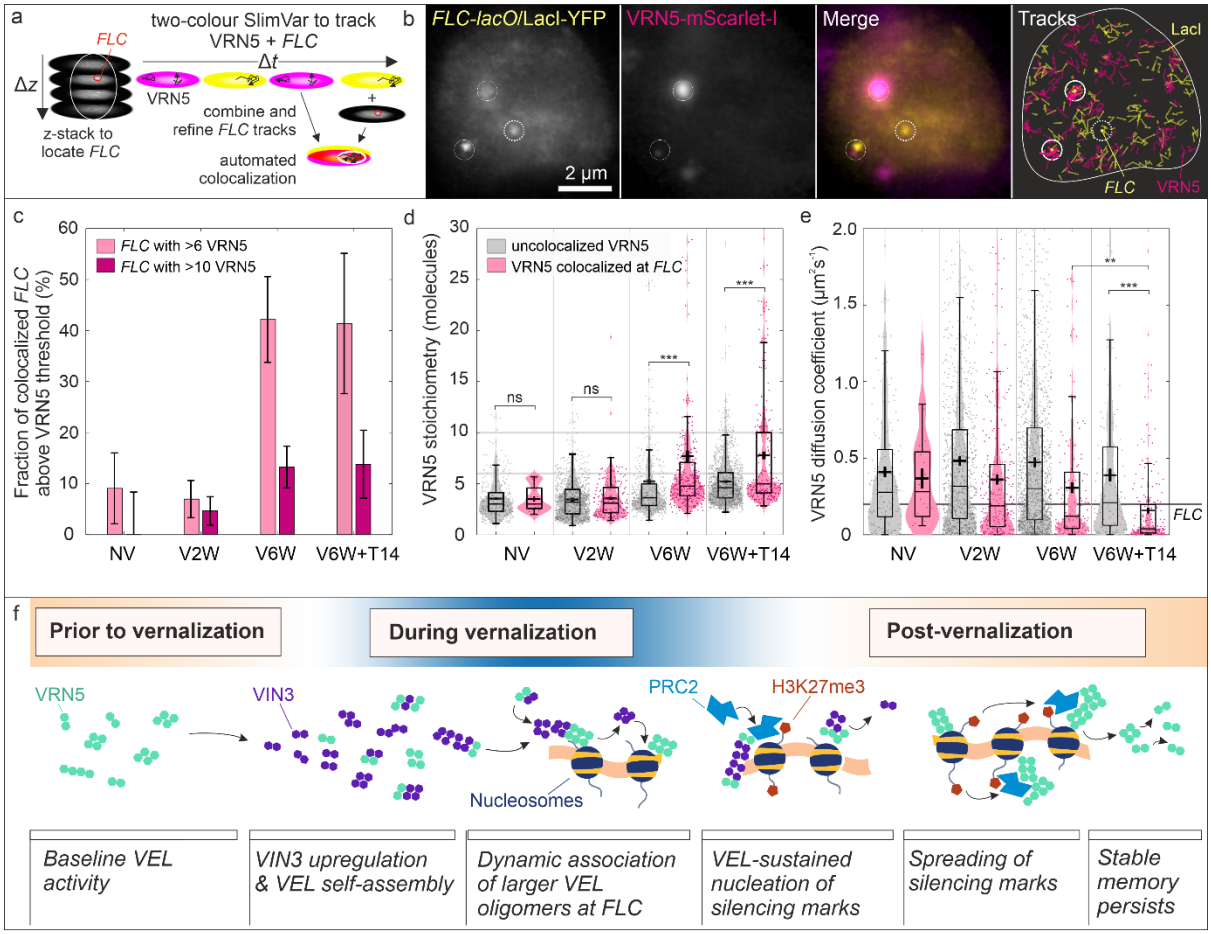

Figure 5. Two-colour SlimVar colocalization analysis reveals a dynamic subset of enlarged VRN5 assemblies present at *FLC* loci after long cold exposure- and after return to warm.

a) Representative example of a z-stack used to screen for *FLC* loci in the LacI-YFP channel, followed by b) two-colour alternating excitation at a single target z-plane to capture *FLC* loci (circles) and colocalization events (solid circles) between *FLC* (yellow) and VRN5-mScI assemblies (magenta) at V6W, as determined by automated tracking analysis (Methods); c) The fraction of *FLC* colocalized with VRN5 stoichiometry above a set threshold increases with vernalization. Total number of detected *FLC* (Supplementary Table 2) found to be colocalized with VRN5 are: (NV) 11, (V2W) 43, (V6W) 83, (V6W+T14) 29. Thresholds are set at which dependence on vernalization becomes statistically significant (>10 molecules) or maximal (>6 molecules). Just (NV) 1/11 and (V2W) 3/43 *FLC* have >6 VRN5 molecules, while this frequency rises with vernalization to (V6W) 35/83 and (V6W+T14) 12/29 *FLC*. At six weeks' cold, the frequency of *FLC* with >6 VRN5 molecules exceeds an average of one transgene per nucleus. d) The mean stoichiometry of colocalized VRN5 exceeds that of uncolocalized VRN5 as a consequence of vernalization. The difference is initially negligible before vernalization (3.5 ± 0.3 vs 3.5 ± 0.1, NS, p=0.39, N=365) but appears clearly at V6W (7.7 ± 0.6 vs 5.0 ± 0.2, p<0.0001***, N=2867) and is sustained for at least two weeks after return to warm (7.8 ± 0.5 vs 5.2 ± 0.2, p<0.0001***, N=1416). e) The diffusivity of VRN5-mScI tracks either colocalized to *FLC* (decreasing with vernalization) or independent of *FLC.* f) Model showing VEL protein dynamic self-assembly and function in vernalization-driven epigenetic silencing.

Both the number and stoichiometry of VRN5 assemblies were considerably lower in this single-copy VRN5-mScI line than in the multiple-copy VRN5-YFP line (Fig. 2c). Like VRN5-YFP, however, these VRN5 assemblies showed stoichiometries that increased with vernalization independent of colocalization at *FLC* (Fig. 5d, grey). There was a proportionally far greater increase in stoichiometry of VRN5 assemblies colocalized at *FLC,* particularly after long cold exposure and after the return to warm (Fig. 5d, magenta). At timepoints prior to and after short cold exposure, the mobility of the colocalized VRN5 assemblies exceeded that typical of *FLC* loci by a factor of ~3, indicating extremely short-lived binding relative to the ~10 ms measurement timescale. After longer cold, the mobility of colocalized VRN5 more closely matched the typical diffusion rate of *FLC* loci, potentially pointing to a tighter interaction (Fig. 5e). Notably, the fraction of VRN5 not colocalized at *FLC* remained at the higher diffusivity independent of vernalization. An interesting, unexpected observation was the high rate of turnover; the colocalization dwell time of individual VRN5 assemblies at *FLC* remained transient, albeit increasing with vernalization, limited to a typical dwell time of ~100 ms.

In Lövkvist et al., 2021 [14], an assembly size of 17 was predicted as the best fit to observations of nucleating silencing marks, potentially reducing further in the case of maximal positive cooperativity. Although we do not know whether VIN3 assemblies colocalize specifically with *FLC*, and if so, the size of such an assembly, a large minority of observed VIN3 and VRN5 assemblies with sufficiently low mobility to interact with *FLC* clearly do exceed this size threshold during and after vernalization. In the case of VRN5, we show this is exceeded by a small minority of assemblies directly colocalized with *FLC* only after vernalization, though at a single gene copy, the maximal distinction with uncolocalized assemblies occurs at even lower thresholds of as low as 6–10 molecules. This finding suggests that if any lower bound size is required for positive feedback to become active in these colocalized assemblies, it must be very low.

Discussion

Here, we have developed a new optical microscopy pipeline—SlimVar—and applied it to image cell nuclei in *Arabidopsis* root tips. SlimVar enables direct detection of rapidly diffusing molecular assemblies in comparatively deep, multicellular samples, by sampling faster than the typical motion of nuclear assemblies, and by its optimising its sensitivity to single fluorescent proteins. Also, SlimVar does not require complex protocols for chemically conjugating target biomolecules. In animal tissues, studies using HILO [45] [56], lightsheet [57] [58] or lattice lightsheet [32] have previously demonstrated single-molecule tracking to a standard of 50 ms sampling at ~300 µm depth, or 10 ms at ~30 µm depth using dyes, which is comparable to SlimVar with fluorescent proteins. However, in plant tissues, single particle tracking at molecular sensitivity has been demonstrated with TIRF [59], [60], or VAEM [28], [30], [61], [62] only in the vicinity of a surface cell layer. SlimVar therefore advances the ability to track and count single-molecular assemblies in plants, and potentially in a range of tissues, to that of more complex existing microscopy technologies.

In achieving this speed, SlimVar trades off some of its 3D capability; the detection of foci is restricted to a limited depth of field much smaller than the nucleus. Nonetheless, it is capable of z-stacks as used here for systematic *FLC* detection, and it should be possible to

extend oblique angle [48] or light sheet-based approaches to achieve rapid volumetric scans [63] and extended depth of field [64]. The implementation of optimal index-matching and photon-efficient adaptive optics [33], [65] could also improve the range of accessible depths while also mitigating the required adjustments for each depth. Single-molecule experimental schemes related to SlimVar such as multiple-colour or photoconvertible labelling on the same target [66], may provide promising future avenues to test this turnover experimentally.

Using SlimVar, we demonstrated oligomeric assemblies of the PRC2 accessory proteins VIN3 and VRN5. VIN3 and VRN5 assemblies increase in stoichiometry above a demonstrable threshold during prolonged cold. Both sets of assemblies exhibit mobility signatures similar to *FLC* gene loci, with a subset of larger VRN5 assemblies clearly demonstrating *FLC* colocalization. The larger assemblies are therefore prime candidates to contribute to memory element function predicted in a hybrid model coupling protein self-assembly and histone modification [14]. Our observation that adding more protein subunits preferentially results in a larger average assembly stoichiometry, rather than a greater number of assemblies, is itself consistent with a model of positive cooperativity. Taken together, these findings support the view that VIN3 and VRN5 assemblies mediate epigenetic memory over the extended vernalization cycle of several weeks (Fig 5f).

The model [14] makes no predictions as to the underpinning factors and mechanisms - neither for protein self-assembly, nor dynamic exchange with the surrounding nucleoplasm. The head-to-tail polymerization via the VEL domain [19] is likely involved, but the predominantly transient interactions between most individual VEL protein assemblies and *FLC* may suggest that the physical feedback processes are more complex than currently understood. Our current interpretation is that the VRN5 assemblies enriched at *FLC*, of sufficient size to satisfy the model, are most likely simple oligomers. Yet, we contemplate whether the very largest of these (~100 VRN5) are instead small dynamic phase separated condensates, related to those observed during transient overexpression of VEL proteins [16], [19], [67]. If so, the collective, multivalent interactions characteristic of condensates might offer a longer, or otherwise more effective, residence time at *FLC* than we observed for typical molecular assemblies, and therefore a disproportionate contribution to epigenetic memory. SlimVar is an excellent tool capable and primed to further investigate these rare mechanistic events *in vivo*.

While pioneered for the Arabidopsis *FLC* system, these protein-mediated feedback processes may underpin Polycomb-based epigenetic memory common to all eukaryotic systems. Our study here, using highly interdisciplinary approaches, demonstrates the value of developing new high precision bioimaging technologies to tackle outstanding biological questions in epigenetic processing and memory storage. Although optimised for applications in *Arabidopsis* root tips, SlimVar is comparatively straightforward and cost-effective to implement with minor modifications to a standard inverted optical microscope, and as such may have future applications in democratizing functional bioimaging research at the molecular scale inside a range of living tissues.

Methods

Plant material and growth conditions

The VIN3-GFP and VRN5-YFP lines have previously been described [8], [16]. To generate the VIN3-SYFP2 line, the GFP of the pENTR pVIN3::VIN3-GFP construct [68] was replaced by SYFP2 by seamless mega-primer cloning. VIN3-SYFP2 was cloned to the SLJ destination vector, a derivative of SLJ755I5 [69] and transformed to *Agrobacterium tumefaciens* C58 by triparental mating. The transgenic VIN3-SYFP2 plant in Col*FRI* background was generated by floral dipping with *Agrobacterium*. To generate pENTR pVRN5::VRN5-mScarlet-I, the SYFP2 of VRN5-SYFP2 [67] was replaced by mScarlet-I by seamless mega-primer cloning. The VRN5-mScarlet-I was cloned to the SLJ destination vector, a derivative of SLJ6991 [69], transformed to *Agrobacterium tumefaciens* C58 and subsequently transferred into *vrn5-8 FRI* mutants as described above. All primers used in this study are listed in Supplementary Table 1. Transgene copy number was determined in T1 or T2 transformants by IDna Genetics (Norwich Research Park). To generate the plant co-expressing VRN5-mScarlet-I and *FLC-lacO*/LacI-YFP, the VRN5-mScarlet-I line was crossed into the *FLC-lacO*/*lacI-YFP* line [53] and was selected by antibiotics.

All seeds were surface-sterilized and sown on 100 mm growth plates containing Murashige and Skoog (MS) medium (Duchefa) with 1 wt. % agar (Difco Bacto) without sucrose. The plates were sealed with Micropore tape (3M) and kept at 4°C in the dark for 2–3 days to stratify the seeds. Plates were racked vertically in the growth chamber in warm conditions (16 h light/ 8 h dark with constant 22 ± 2°C, 60 ± 10% Relative Humidity (RH)) for 7 days. Non-vernalized timepoints (NV) were then imaged on the final day. For all other timepoints, plants were grown in warm conditions for 7 days as above and then were transferred to cold conditions (8h light / 16h dark, 5 ± 1°C, 50 ± 30 % RH) to vernalize for either 2 or 6 weeks (V2W and V6W respectively). Following vernalization, a subset of plates was returned to warm conditions for an additional period of either 7 or 14 days (V6W+T7 or V6W+T14). Plates for warm timepoints (NV, V6W+T7, V6W+T14) were handled at room temperature, while those imaged at cold timepoints (V2W and V6W) were transferred on ice to a 4°C cold room for slide preparation to avoid temperature spikes affecting the fragile vernalized state. All VIN3 imaging was performed in daylight hours 4–7 to align with the diurnal maximum in VIN3 expression [7]. At least 3 independent vernalization courses were grown for each line and timepoint (Supplementary Table 2).

Immediately prior to imaging the *FLC-lacO*/LacI-YFP lines (single colour or dually labelled with VRN5-mScarlet-I), LacI-YFP was induced by placing opened growth plates next to a bath of 0.5% EtOH at 25°C in an airtight container for 2.5 h. This resulted in an optimal amount of LacI-YFP expression in the meristem for SlimVar imaging without spot-bleaching, below the near-saturated induction level (1.5–2% EtOH for 1.5 h [53]) used for confocal study (Supplementary Figure 6a).

RNA expression analysis

Total RNA was extracted using the phenol method as previously described [8], [70]. Genomic DNA was removed from the TURBO DNA-free kit (Invitrogen, AM1907) before reverse transcription with SuperScript IV reverse transcriptase (Invitrogen, 18090050) and

gene-specific primers. Quantitative PCR analysis was performed on a LightCycler480 II (Roche). Target gene expression was normalized by PP2A (AT1G13320) and UBC (AT5G25760). All primers used in this study are listed in Supplementary Table 1.

Preparation of samples for imaging

Identical slides were prepared for confocal, Airyscan or SlimVar imaging [45]. Briefly, GeneFrames (Thermo Scientific, AB0578) were affixed to standard slides (VWR) and filled with MS medium plus 1 wt.% agarose to produce agar pads. Where necessary due to seedling size, the terminal >10mm of the primary root of each plant was excised using a razor. Root tips were laid on each agar pad with tweezers. Liquid MS media was applied to exclude air and each slide was sealed with a plasma-cleaned #1.5 coverslip (VWR). Each slide was imaged within <1h.

Confocal and Airyscan imaging

Confocal imaging was performed on a Zeiss LSM880 microscope equipped with argon ion laser and Plan-Apochromat 63×/1.40 NA oil objective lens (Zeiss). Samples were illuminated at 488 or 514 nm (GFP or YFP/SYFP2 channels) respectively, and the emission detected in wavebands 490-550 nm or 518-550 nm respectively [45]. The root tip confocal images (Fig 1b, Supplementary Figure 1, Supplementary Figure 6a-d) were acquired as z-stacks over ≤3 z-slices of 1000 × 1000 pixels at 0.6× zoom factor, at 1.5 µm intervals using 20 mW excitation power. Slices were postprocessed in FIJI/ImageJ [71] with a 2D median filter (0.2 µm filter size) to suppress noise before performing a mean z-projection.

Timelapse z-stacks of nuclei (Fig. 1c) were acquired in Airyscan RS mode, after aligning the detector with immobilised TetraSpeck microspheres (Invitrogen, 0.1 µm diameter). Each sequence contained ≤25 volumetric cycles, each taking 0.84 s (12 slices × 56 ms/slice). The axial step size was 0.65 µm with 112 × 112 pixels at 14× zoom factor and 20mW excitation power. The 3D z-stacks were Airyscan post-processed in Zen Black software (Zeiss) with a user-optimised strength parameter of 5.0. Vernalized timepoints (V2W, V6W) were imaged at 5 ± 1 °C on a water-recirculating Peltier-cooled stage (Linkam PE100) calibrated using hydrocarbon melting points.

SlimVar imaging

The SlimVar platform was adapted from a Slimfield microscope consisting of an objective-lens-based total internal reflection fluorescence setup, custom-built from benchtop optical components (Thorlabs). A general scheme of Slimfield microscopy is available [40], [41], [72] with key terms defined in Table 2 [73].

With increasing acquisition depth, refractive index mismatch between immersion oil and aqueous sample is a key challenge [74] due to spherical aberration and excitation beam deviations. This can be largely avoided with expensive water or silicone immersion objective lenses specialised for TIRF, but to demonstrate affordable and accessible performance, we used a widely available oil immersion lens: NA 1.49 Apo TIRF 100× oil immersion objective lens (Nikon). Single molecule sensitivity was afforded by a fast sCMOS camera (Teledyne Photometrics Prime95B, 12-bit 'Sensitivity' gain). A 580 nm longpass beamsplitter enabled simultaneous detection of GFP (525/50 nm centre/bandwidth emission filter) or YFP (550/25 nm) in a green/yellow channel, and mScarletI (594/25 nm) in

a red channel. The total magnification was ~200× giving an oversampled pixel width of 53 nm.

Continuous wave lasers (Coherent OBIS) delivered Gaussian beams (TEM_{00}) at 488 nm, 514 nm and 561 nm that were circularised by quarter waveplate [75], de-expanded, then focused at the objective back aperture to collimate them through the sample. SlimVar featured an oblique beam angle similar to HILO [48], PaTCH [76] and VAEM [48], [49]. To optimise background contrast for *Arabidopsis* root tips, a four-step calibration was performed:

i) the second convex lens in the expansion telescope was mounted on a lateral translation stage with a high-precision micrometer; this shift (up to 2.3 mm) generated an equivalent lateral displacement of the beam at the 6 mm diameter objective back aperture, thereby tilting the beam away from the optic axis at the sample. The beam delivery angle was calibrated for lens micrometer position following [78] and set to 50° ± 3° from normal incidence in oil, corresponding to 60° ± 5° in water by Snell's Law, with minimal coupling into the evanescent field at the coverslip.

ii) a field stop was placed in the conjugate plane upstream of the first telescope lens. Rather than thinning the beam with rectangular slits to further suppress background [49], we chose to maintain a circular beam; this illuminated the full depth of each nucleus for representative estimates of nuclear protein copy and efficient screening of *FLC* loci. The stop was tightened to crop the beam (Gaussian $1/e^2$ diameter of 17 µm) to between 4–9 µm cross-section. The field then approximated an ellipse of $1 \times 3^{1/2}$ the chosen beam cross-section, or 4–16 µm diameter, uniformly illuminated at a power density of 1–5 kW cm^{-2}, which matched the saturation excitation intensity of the fluorescent proteins.

iii) a pair of mirrors were used to incline the beam ~5 mrad from the optic axis at the objective back aperture, to compensate the beam's mismatch-dependent lateral deflection of ~11 µm at the 20 µm calibration depth.

iv) the objective correction collar was adjusted to compensate spherical aberration at the calibration depth for a minimal FWHM of detected foci ~170 nm (Fig. 1d) and a localization precision [79] of 40 nm (Supplementary Fig. 8) within live roots.

The net increase in median signal-to-noise ratio (when normalised by the square root of exposure time × excitation power) due to the above beam angle optimisation was in the range 2.5–3.3 (n = 500 foci).

Nuclei were identified in brightfield to find best focus—typically the nucleolar midbody—without any photobleaching, and were captured for manual segmentation. Fluorescence acquisition settings in green, yellow and/or red channels were pre-optimised to avoid initial camera saturation and to ensure detection of individual tracks of molecular brightness for GFP, SYFP2 / YFP, and mScarlet-I respectively. Three exposure times were used: i) a 'representative' 20 ms providing a low-bias detection of all particles down to single molecules, ii) 'fast' 2 ms to ensure robustness of tracking fidelity and mobility measurements of only the brightest assemblies, and iii) a 'balanced' 10 ms, also capable of single molecule detection. Fast acquisitions captured the subset of assemblies with fourfold (upper quartile) mean stoichiometry at a tripled detection rate due to the faster sampling bandwidth. Results shown derive from data collected with the representative (VRN5-YFP

and VIN3-GFP lines) or balanced mode (VIN3-SYFP2, *FLC-lacO*/LacI-YFP and VRN5-mScarlet-I lines) unless otherwise stated. These settings were fixed to minimize systematic variation in the characteristic single molecule brightness (Supplementary Fig. 5).

The region of interest spanned ≤300 rows (16 µm) giving a readout time of 2.7 ms per frame, and sampling rates of 44–217 fps. Lasers were triggered in each frame by the camera in 'All Rows' mode to provide global shuttering without extraneous photobleaching. For dual colour colocalization, 514 nm and 561 nm lasers were excited in alternating frames (ALEX) to facilitate distinct signals for each reporter. To capture photoblinking, the number of frames in each sequence was set to >50× the photobleaching decay constant.

Metric / Object	Definition
Focus (foci)	A spot-like local intensity maximum in a single frame, which corresponds to a localized group of labelled molecules. Associated properties include spatial location, total intensity, and signal-to-noise ratio.
Track	A set of foci in adjacent frames which are spatially close enough to form a trajectory.
Characteristic single-molecule brightness	The average number of pixel counts in foci associated with a single fluorescent reporter molecule (e.g. GFP), under a fixed imaging condition. Equivalent to the modal step size in intensity for tracks in the final stage of photobleaching.
Integrated nuclear intensity	The total fluorescence intensity of an entire nuclear segment in pixel counts, normalised by the characteristic single molecule brightness.
Nuclear protein copy number	The average number of molecules in a nucleus, as estimated from the increase in integrated nuclear intensity above negative control.
Stoichiometry	The number of labelled molecules in a track, as estimated by dividing the track's initial intensity by the characteristic single-molecule brightness.
Periodicity	The number of labelled molecules in a repeat unit within tracked objects, as estimated by the consistent stoichiometry intervals between nearest-neighbour peaks in the stoichiometry distribution.
Diffusion coefficient	Measure of the random microscopic motion of a track based on the increase in its (mean-squared) displacement over time.

Table 2. Definitions of analysis metrics for single particle tracking.

Protein tracking and intensity analysis

Fluorescent foci in the SlimVar microscope's depth of field were extracted using ADEMScode software [42] with a Gaussian masking algorithm and linked into tracks. The centroid of each focus was localized to super-resolved, subpixel precision [79], typically 40 nm (Supplementary Fig. 8) consistent with best Slimfield performance [80].

The probability of random overlap between similar foci (leading to spurious summation of intensities) was estimated by modelling the probability of nearest neighbour distances in a random Poisson process falling within the widefield localization precision [72]. For the track densities in this study, the estimated fraction of randomly overlapping tracks is no greater

than 10%. Analyses were restricted to the image region of effectively uniform laser illumination (80% ± 9% s.d. peak intensity) no greater than 190 × 300 pixels (10 × 16 µm). Fluorescence sequences were cropped to specify individual nuclei, using masks manually segmented from brightfield images. The 2D diffusion coefficient of each track, D, was estimated according to a random walk model as a quarter of the rate of increase of the mean-squared displacement with lag time [81]. The intensity of each focus was calculated by integrating the pixel value intensity within 5 pixels of each focus and subtracting a background level averaged over the remainder of a 17 × 17-pixel window. The initial intensity of each track was determined by backward extrapolation of the intensities of the first 5 foci to a virgin timepoint prior to photobleaching. The characteristic single molecule brightness corresponding to each fluorescent reporter was determined based on the Chung-Kennedy-filtered [82] terminal intensity of tracks in each acquisition (Supplementary Fig. 5). The characteristic single molecule brightness was 172 ± 15 (counts, mean ± sem) for VIN3-GFP, 126 ± 16 for VRN5-YFP and LacI-YFP, 131 ± 25 for VIN3-SYFP2 and 140 ± 18 for VRN5-mScarlet-I. These values were used for internal calibration of each track stoichiometry (the initial track intensity divided by this single molecule brightness) and each dataset periodicity and nuclear protein copy number. For comparison, *in vitro* values for characteristic single molecule brightness were obtained from *E. coli* recombinant fluorescent proteins at a coverslip surface under the same SlimVar imaging conditions.

Stoichiometry periodicity analysis

To calculate stoichiometry periodicity, first the stoichiometries of all tracks within each nucleus were aggregated across nuclei in a dataset (genotype and vernalization status), then represented as a kernel density distribution. The upper limit for the kernel width was the empirical range on the characteristic single molecule brightness of 0.6 molecules [40]; to avoid oversmoothing, we used the standard deviation of 0.3 molecules. Peaks in this distribution were detected using the MATLAB *findpeaks* function, and the intervals between nearest neighbour peaks were calculated. The uncertainty in peak-to-peak interval was estimated as the single molecule uncertainty of 0.6 molecules multiplied by the square root of the mean stoichiometry, divided by the square root of the number of interpolated intervals [76]. To suppress noise and spurious intra-peak sampling, all peak intervals smaller than the interval uncertainty were discarded. A second kernel density estimate was calculated over the remaining peak intervals, with the interval uncertainty as the kernel width. This curve describes the distribution of peak intervals in the stoichiometry as shown in Fig. 3 (insets) and Supplementary Fig. 3d. The modal value of this interval distribution was reported as the predominant periodicity of assemblies in each dataset. This method of estimating periodicity was verified as independent of the mean stoichiometry using simulated positive control data drawn from noisy Poisson-distributed multiples of an oligomeric ground truth [73]. This analysis reproduced the expectation that the minimum number of tracks required for sufficient peak sampling, and therefore the limit of periodicity detection, scales with the square root of the mean stoichiometry. To demonstrate a negative control, 100 aperiodic sets of 10^4 stoichiometry values, uniformly distributed at random between 1–30 molecules, were generated using the *randperm* MATLAB function

and processed to generate a set of 100 independent interval distribution curves each corresponding to null periodicity. The 95th percentile fraction of peak intervals was calculated at each interval size to generate a null curve, below which test data could no longer be considered periodic. The uncertainty in the reported modal peak interval was estimated as the standard error on the mean (sem) of the peak intervals falling within the range above the null threshold line. The periodicity analysis was validated *in vivo* using the gold standard of tetrameric LacI-YFP [51] detected in the *FLC-lacO*/LacI-YFP lines (Supplementary Fig. 7b).

Raw estimates for the total number of molecules in each nucleus were extracted with an *ImageJ* macro following [42]. The pixel values were integrated within each nuclear segment, then normalized by the characteristic single molecule brightness to give an integrated nuclear intensity in molecular equivalents (Fig. 2a). These values did not account for the additive contribution from autofluorescence background, which we estimated using the corresponding unlabelled control line, Col*FRI*. The nuclear protein copy number of each labelled dataset was refined to exclude autofluorescence by taking the difference between mean integrated nuclear intensities of the labelled dataset and unlabelled control, adjusted in proportion to the ratio of mean areas of nuclear segments. The negative control was much brighter in green acquisitions (15,000 ± 1500 GFP equivalents vs. 3,800 ± 400 YFP/SYFP2; mean ± sem, N=33, N=27 respectively). The nucleoplasmic concentrations were estimated by dividing each nuclear protein copy number by the mean nuclear volume (assuming prolate spheroidal nuclei aligned in the image plane) and multiplying by Avogadro's number.

Colocalization imaging

For each nucleus, a z-stack was performed, first with brightfield imaging to ensure alignment, then with 514 nm wavelength SlimVar excitation at 10 ms/frame exposure to track *FLC* loci via LacI-YFP. This z-range extended from the highest to lowest surface of each nucleus with respect to the coverslip surface, and was divided into equally spaced intervals of 280–360 nm. During each stack, the z-position of the image frame (denoted I*) containing the brightest LacI-YFP focus was noted and subsequently revisited (Fig. 5a). We then performed a dual-colour SlimVar acquisition, 10 ms exposure time alternating between 561 nm and 514 nm excitation wavelengths. The total duration of the fluorescent z-stack and alternating excitation acquisitions for each nucleus was ≤15 s. We estimate that the maximum displacement of *FLC* loci during the 15 s period was within 180 nm, less than our optical resolution limit and consistent with previous observations [83] (Supplementary Fig. 8d), thus in effect immobile over this timescale.

During post-processing, the two colour channels were spatially registered to sub-pixel precision using affine transforms generated from SlimVar images of 200 nm diameter fluorescent beads *in vitro.* Then both yellow and red channel image sequences were tracked independently (Fig 5b) to generate lists of LacI-YFP and VRN5-mScI tracks

respectively. To account for *FLC* candidates observed in the z-stack but photobleached prior to the alternating acquisition, a copy of the alternating sequence was generated in which each yellow channel image simply comprised I*. This copy was also tracked, and its list of LacI-YFP tracks appended to the list from the original sequence. Collected LacI-YFP tracks are shown in Fig 5b (yellow traces)

To exclude false positive detections of *FLC* due to free LacI-YFP, we then selected only slow and bright yellow tracks. Our earlier observations suggest a maximum of 8 *FLC* loci in the entire nucleus (Supplementary Fig. 6). On that basis, we selected the LacI-YFP tracks whose diffusivity was ≤ D_{FLC} (Fig 4a) and from these, retained the 8 brightest (or all if fewer than 8) tracks in each nucleus. These selected *FLC* tracks, typically 1-4 per nucleus (Fig 5b, white circles), were run through colocalization analysis with the corresponding VRN5-mScI tracks (Fig 5b, magenta traces) using a previously reported algorithm [72].

Briefly, VRN5 and *FLC* tracks were deemed colocalized if they met an intensity overlap condition [84] of at least 50% (effectively a lateral distance of ~3 pixels or one widefield localization precision) and remained within a distance of 7 pixels (twice the widefield localization precision) for ≥3 frames. The high numerical aperture and short depth of field ensured an axial precision better than <220 nm FWHM for all colocalizations. The likelihood of false positive overlaps between VRN5 tracks, and the likelihood of false positive colocalizations (an *FLC* locus being colocalized with a VRN5 assembly by random chance) were both <5%, based on the average initial number density of tracks in each frame (5.2 VRN5 and 3.3 candidate *FLC*) distributed in the nucleoplasm under random point statistics [85].

Statistics and samples

All pairwise comparisons used the non-parametric Brunner-Munzel test. Sample size and significance are indicated alongside each result. Investigators were not blinded and each acquisition was independent. We predetermined a target sample size of >24 cells total per line per condition, sufficiently powered to detect changes of <1 s.d. in each of the five test variables (number of tracks, nuclear protein copy number, stoichiometry, periodicity, diffusivity) at a Bonferroni-adjusted significance level of $\alpha = 0.05/5 = 0.01$. We planned biological replicates of >3 independent cycles of growth and vernalization, with >3 roots per cycle and >3 cells per root. In the dual line, >10 cells per condition sufficed for estimates of track number and stoichiometry disaggregated by *FLC* colocalization. Technical replicates were identified with tracks detected within each nuclear segment. Actual numbers of replicates analysed are detailed in Supplementary Table 2.

Data and Code Availability

All raw imaging data and analysed tracks will be made available at the BioImage Archive.

The ADEMScode MATLAB tracking analysis software can be found at https://github.com/alex-payne-dwyer/single-molecule-tools-alpd.

References

[1] G. Cavalli and E. Heard, “Advances in epigenetics link genetics to the environment and disease,” *Nature*, vol. 571, no. 7766, pp. 489–499, 2019, doi: 10.1038/s41586-019-1411-0.

[2] J. Müller and J. A. Kassis, “Polycomb response elements and targeting of Polycomb group proteins in Drosophila,” *Curr Opin Genet Dev*, vol. 16, no. 5, pp. 476–484, Oct. 2006, doi: 10.1016/j.gde.2006.08.005.

[3] R. T. Coleman and G. Struhl, “Causal role for inheritance of H3K27me3 in maintaining the off state of a Drosophila HOX gene,” *Science*, vol. 356, no. 6333, p. eaai8236, 2017, doi: 10.1126/science.aai8236.

[4] N. P. Blackledge and R. J. Klose, “The molecular principles of gene regulation by Polycomb repressive complexes,” *Nat Rev Mol Cell Biol*, vol. 22, no. 12, pp. 815–833, Dec. 2021, doi: 10.1038/s41580-021-00398-y.

[5] G. Menon, A. Schulten, C. Dean, and M. Howard, “Digital paradigm for Polycomb epigenetic switching and memory,” *Curr Opin Plant Biol*, vol. 61, p. 102012, Jun. 2021, doi: 10.1016/j.pbi.2021.102012.

[6] J. Hepworth *et al.*, “Absence of warmth permits epigenetic memory of winter in Arabidopsis,” *Nature Communications*, vol. 9, no. 1, p. 639, 2018, doi: 10.1038/s41467-018-03065-7.

[7] R. L. Antoniou-Kourounioti *et al.*, “Temperature Sensing Is Distributed throughout the Regulatory Network that Controls FLC Epigenetic Silencing in Vernalization,” *Cell Systems*, vol. 7, no. 6, pp. 643–655, 2018, doi: 10.1016/j.cels.2018.10.011.

[8] H. Yang, S. Berry, T. S. G. Olsson, M. Hartley, M. Howard, and C. Dean, “Distinct phases of Polycomb silencing to hold epigenetic memory of cold in Arabidopsis,” *Science*, vol. 357, no. 6356, pp. 1142–1145, 2017, doi: 10.1126/science.aan1121.

[9] A. Angel, J. Song, H. Yang, J. I. Questa, C. Dean, and M. Howard, “Vernalizing cold is registered digitally at FLC,” *Proc Natl Acad Sci U S A*, vol. 112, no. 13, pp. 4146–4151, Mar. 2015, doi: 10.1073/pnas.1503100112.

[10] S. Costa and C. Dean, “Storing memories: The distinct phases of Polycomb-mediated silencing of Arabidopsis FLC,” *Biochemical Society Transactions*, vol. 47, no. 4, pp. 1187–1196, 2019, doi: 10.1042/BST20190255.

[11] S. Berry, M. Hartley, T. S. G. Olsson, C. Dean, and M. Howard, “Local chromatin environment of a Polycomb target gene instructs its own epigenetic inheritance,” *eLife*, vol. 4, p. e07205, 2015, doi: 10.7554/eLife.07205.

[12] J. S. Mylne *et al.*, “LHP1, the Arabidopsis homologue of HETEROCHROMATIN PROTEIN1, is required for epigenetic silencing of FLC,” *Proceedings of the National Academy of Sciences of the United States of America*, vol. 103, no. 13, pp. 5012–7, 2006, doi: 10.1073/pnas.0507427103.

[13] D. S. Saxton and J. Rine, “Epigenetic memory independent of symmetric histone inheritance,” *eLife*, vol. 8, pp. 1–44, 2019, doi: 10.7554/eLife.51421.

[14] C. Lövkvist, P. Mikulski, S. Reeck, M. Hartley, C. Dean, and M. Howard, “Hybrid protein assembly-histone modification mechanism for PRC2-based epigenetic switching and memory,” *eLife*, vol. 10, p. e66454, 2021, doi: 10.7554/eLife.66454.

[15] A. Laugesen, J. W. Højfeldt, and K. Helin, “Molecular Mechanisms Directing PRC2 Recruitment and H3K27 Methylation,” *Molecular Cell*, vol. 74, no. 1, pp. 8–18, 2019, doi: 10.1016/j.molcel.2019.03.011.

[16] T. Greb *et al.*, “The PHD Finger Protein VRN5 Functions in the Epigenetic Silencing of Arabidopsis FLC,” *Current Biology*, vol. 17, no. 1, pp. 73–78, 2007, doi: 10.1016/j.cub.2006.11.052.

[17] S. Sung and R. M. Amasino, “Vernalization in Arabidopsis thaliana is mediated by the PHD finger protein VIN3,” *Nature*, vol. 427, no. 6970, pp. 159–64, 2004, doi: 10.1038/nature02195.

[18] D. H. Kim and S. Sung, “Coordination of the vernalization response through a VIN3 and FLC gene family regulatory network in Arabidopsis,” *Plant Cell*, vol. 25, no. 2, pp. 454–69, 2013, doi: 10.1105/tpc.112.104760.

[19] M. Fiedler *et al.*, “Head-to-tail polymerization by VEL proteins underpins cold-induced Polycomb silencing in flowering control,” *Cell Rep*, vol. 41, no. 6, p. 111607, Nov. 2022, doi: 10.1016/j.celrep.2022.111607.

[20] E. Franco-Echevarría, T. J. Rutherford, M. Fiedler, C. Dean, and M. Bienz, “Plant vernalization proteins contain unusual PHD superdomains without histone H3 binding activity,” *Journal of Biological Chemistry*, vol. 298, no. 11, Nov. 2022, doi: 10.1016/j.jbc.2022.102540.

[21] P. K. Hepler and B. E. S. Gunning, “Confocal fluorescence microscopy of plant cells,” *Protoplasma*, vol. 201, no. 3, pp. 121–157, Sep. 1998, doi: 10.1007/BF01287411.

[22] S. L. Shaw, D. Thoms, and J. Powers, “Structured illumination approaches for super-resolution in plant cells,” *Microscopy (Oxf)*, vol. 68, no. 1, pp. 37–44, Feb. 2019, doi: 10.1093/jmicro/dfy043.

[23] M. Ovecka *et al.*, “Imaging plant cells and organs with light-sheet and super-resolution microscopy,” *Plant Physiology*, vol. 188, no. 2, pp. 683–702, 2022, doi: 10.1093/plphys/kiab349.

[24] A. Y. Guo, Y. M. Zhang, L. Wang, D. Bai, Y. P. Xu, and W. Q. Wu, “Single-molecule imaging in living plant cells: A methodological review,” *International Journal of Molecular Sciences*, vol. 22, no. 10, p. 5071, 2021, doi: 10.3390/ijms22105071.

[25] T. Dumur *et al.*, “Probing the 3D architecture of the plant nucleus with microscopy approaches: challenges and solutions,” *Nucleus*, vol. 10, no. 1, pp. 181–212, 2019, doi: 10.1080/19491034.2019.1644592.

[26] L. Colin *et al.*, “Imaging the living plant cell: From probes to quantification,” *Plant Cell*, vol. 34, no. 1, pp. 247–272, 2022, doi: 10.1093/plcell/koab237.

[27] X. Wang, X. Li, X. Deng, D. T. Luu, C. Maurel, and J. Lin, “Single-molecule fluorescence imaging to quantify membrane protein dynamics and oligomerization in living plant cells,” *Nature Protocols*, vol. 10, no. 12, pp. 2054–63, 2015, doi: 10.1038/nprot.2015.132.

[28] Y. Cui, M. Yu, X. Yao, J. Xing, J. Lin, and X. Li, “Single-Particle Tracking for the Quantification of Membrane Protein Dynamics in Living Plant Cells,” *Molecular Plant*, vol. 11, no. 11, pp. 1315–1327, 2018, doi: 10.1016/j.molp.2018.09.008.

[29] N. Prunet and K. Duncan, “Imaging flowers: a guide to current microscopy and tomography techniques to study flower development,” *Journal of Experimental Botany*, vol. 71, no. 10, pp. 2898–2909, May 2020, doi: 10.1093/jxb/eraa094.

[30] M. P. Platre *et al.*, “Developmental control of plant Rho GTPase nano-organization by the lipid phosphatidylserine,” *Science*, vol. 364, no. 6435, pp. 57–62, Apr. 2019, doi: 10.1126/science.aav9959.

[31] X. Zhang, Y. Cui, M. Yu, and J. Lin, “Single-Molecule Techniques for Imaging Exo-Endocytosis Coupling in Cells,” *Trends Plant Sci*, vol. 24, no. 9, pp. 879–880, Sep. 2019, doi: 10.1016/j.tplants.2019.05.013.

[32] B.-C. Chen *et al.*, “Lattice light-sheet microscopy: Imaging molecules to embryos at high spatiotemporal resolution,” *Science*, vol. 346, no. 6208, p. 1257998, Oct. 2014, doi: 10.1126/science.1257998.

[33] T.-L. Liu *et al.*, “Observing the cell in its native state: Imaging subcellular dynamics in multicellular organisms,” *Science*, vol. 360, no. 6386, p. eaaq1392, Apr. 2018, doi: 10.1126/science.aaq1392.

[34] R. Schmidt *et al.*, “MINFLUX nanometer-scale 3D imaging and microsecond-range tracking on a common fluorescence microscope,” *Nat Commun*, vol. 12, p. 1478, Mar. 2021, doi: 10.1038/s41467-021-21652-z.

[35] T. Deguchi *et al.*, “Direct observation of motor protein stepping in living cells using MINFLUX,” *Science*, vol. 379, no. 6636, pp. 1010–1015, Mar. 2023, doi: 10.1126/science.ade2676.

[36] V. Bayle *et al.*, “Single-particle tracking photoactivated localization microscopy of membrane proteins in living plant tissues,” *Nature Protocols*, vol. 16, no. 3, pp. 1600–1628, 2021, doi: 10.1038/s41596-020-00471-4.

[37] M. Lummer, F. Humpert, M. Wiedenlübbert, M. Sauer, M. Schüttpelz, and D. Staiger, “A New Set of Reversibly Photoswitchable Fluorescent Proteins for Use in Transgenic Plants,” *Molecular Plant*, vol. 6, no. 5, pp. 1518–1530, Sep. 2013, doi: 10.1093/MP/SST040.

[38] R. J. Iwatate *et al.*, “Covalent Self-labeling of tagged proteins with chemical fluorescent dyes in BY-2 cells and arabidopsis seedlings,” *Plant Cell*, vol. 32, no. 10, pp. 3081–3094, 2020, doi: 10.1105/tpc.20.00439.

[39] N. Yagi, A. Yoshinari, R. J. Iwatate, R. Isoda, W. B. Frommer, and M. Nakamura, “Advances in Synthetic Fluorescent Probe Labeling for Live-Cell Imaging in Plants,” *Plant and Cell Physiology*, vol. 62, no. 8, pp. 1259–1268, 2021, doi: 10.1093/pcp/pcab104.

[40] M. C. Leake, J. H. Chandler, G. H. Wadhams, F. Bai, R. M. Berry, and J. P. Armitage, “Stoichiometry and turnover in single, functioning membrane protein complexes,” *Nature*, vol. 443, no. 7109, pp. 355–358, 2006, doi: 10.1038/nature05135.

[41] M. Plank, G. H. Wadhams, and M. C. Leake, “Millisecond timescale slimfield imaging and automated quantification of single fluorescent protein molecules for use in probing complex biological processes,” *Integrative Biology*, vol. 1, no. 10, pp. 602–612, 2009, doi: 10.1039/b907837a.

[42] A. J. M. Wollman and M. C. Leake, “Millisecond single-molecule localization microscopy combined with convolution analysis and automated image segmentation to determine protein concentrations in complexly structured, functional cells, one cell at a time,” *Faraday Discussions*, vol. 184, pp. 401–424, 2015, doi: 10.1039/C5FD00077G.

[43] H. Miller *et al.*, “High-speed single-molecule tracking of CXCL13 in the B-follicle,” *Frontiers in Immunology*, vol. 9, p. 1073, 2018, doi: 10.3389/fimmu.2018.01073.

[44] J. I. Qüesta *et al.*, “Noncoding SNPs influence a distinct phase of Polycomb silencing to destabilize long-term epigenetic memory at Arabidopsis FLC,” *Genes and Development*, vol. 34, no. 5, pp. 446–461, 2020, doi: 10.1101/gad.333245.119.

[45] A. L. Payne-Dwyer and M. C. Leake, “Single-molecular quantification of flowering control proteins within nuclear condensates in live whole Arabidopsis root,” in *Chromosome Architecture: Methods in Molecular Biology*, M. C. Leake, Ed., New York, NY: Springer US, Humana, 2022, p. 2476. doi: 10.1007/978-1-0716-2221-6.

[46] T. A. Dittmer, N. J. Stacey, K. Sugimoto-Shirasu, and E. J. Richards, “LITTLE NUCLEI genes affecting nuclear morphology in Arabidopsis thaliana,” *Plant Cell*, vol. 19, no. 9, pp. 2793–2803, Sep. 2007, doi: 10.1105/tpc.107.053231.

[47] C. A. Konopka and S. Y. Bednarek, “Variable-angle epifluorescence microscopy: A new way to look at protein dynamics in the plant cell cortex,” *Plant Journal*, vol. 53, no. 1, pp. 186–96, 2008, doi: 10.1111/j.1365-313X.2007.03306.x.

[48] M. Tokunaga, N. Imamoto, and K. Sakata-Sogawa, “Highly inclined thin illumination enables clear single-molecule imaging in cells,” *Nature Methods*, vol. 5, no. 2, pp. 159–61, 2008, doi: 10.1038/nmeth1171.

[49] L. Gardini, T. Vignolini, V. Curcio, F. S. Pavone, and M. Capitanio, “Optimization of highly inclined illumination for diffraction-limited and super-resolution microscopy,” *Opt Express*, vol. 31, no. 16, pp. 26208–26225, Jul. 2023, doi: 10.1364/OE.492152.

[50] L. Adler *et al.*, “The role of BST4 in the pyrenoid of Chlamydomonas reinhardtii,” *bioRxiv*, p. 2023.06.15.545204, Nov. 2023, doi: 10.1101/2023.06.15.545204.

[51] M. Lewis *et al.*, “Crystal structure of the lactose operon repressor and its complexes with DNA and inducer,” *Science*, vol. 271, no. 5253, pp. 1247–1254, Mar. 1996, doi: 10.1126/science.271.5253.1247.

[52] A. J. M. Wollman *et al.*, “Tetrameric UvrD Helicase Is Located at the E. Coli Replisome due to Frequent Replication Blocks,” *J Mol Biol*, vol. 436, no. 2, p. 168369, Jan. 2024, doi: 10.1016/j.jmb.2023.168369.

[53] S. Rosa *et al.*, “Physical clustering of FLC alleles during polycomb-mediated epigenetic silencing in vernalization,” *Genes and Development*, vol. 27, no. 17, pp. 1845–50, 2013, doi: 10.1101/gad.221713.113.

[54] A.-M. Ladouceur *et al.*, “Clusters of bacterial RNA polymerase are biomolecular condensates that assemble through liquid-liquid phase separation,” *Proc Natl Acad Sci U S A*, vol. 117, no. 31, pp. 18540–18549, Aug. 2020, doi: 10.1073/pnas.2005019117.

[55] D. S. Bindels *et al.*, “mScarlet: a bright monomeric red fluorescent protein for cellular imaging,” *Nat Methods*, vol. 14, no. 1, pp. 53–56, Jan. 2017, doi: 10.1038/nmeth.4074.

[56] H. Zhan *et al.*, “In vivo single-molecule imaging identifies altered dynamics of calcium channels in dystrophin-mutant C. elegans,” *Nat Commun*, vol. 5, no. 1, p. 4974, Sep. 2014, doi: 10.1038/ncomms5974.

[57] J. G. Ritter, R. Veith, A. Veenendaal, J. P. Siebrasse, and U. Kubitscheck, “Light Sheet Microscopy for Single Molecule Tracking in Living Tissue,” *PLOS ONE*, vol. 5, no. 7, p. e11639, Jul. 2010, doi: 10.1371/journal.pone.0011639.

[58] M. Reisser, A. Palmer, A. P. Popp, C. Jahn, G. Weidinger, and J. C. M. Gebhardt, “Single-molecule imaging correlates decreasing nuclear volume with increasing TF-chromatin associations during zebrafish development,” *Nat Commun*, vol. 9, no. 1, p. 5218, Dec. 2018, doi: 10.1038/s41467-018-07731-8.

[59] X. Li *et al.*, “Single-Molecule Analysis of PIP2;1 Dynamics and Partitioning Reveals Multiple Modes of Arabidopsis Plasma Membrane Aquaporin Regulation[C][W],” *Plant Cell*, vol. 23, no. 10, pp. 3780–3797, Oct. 2011, doi: 10.1105/tpc.111.091454.

[60] K. Song, Y. Xue, X. Wang, Y. Wan, X. Deng, and J. Lin, “A modified GFP facilitates counting membrane protein subunits by step-wise photobleaching in *Arabidopsis*,” *Journal of Plant Physiology*, vol. 213, pp. 129–133, Jun. 2017, doi: 10.1016/j.jplph.2017.03.009.

[61] C. Pain, C. Tynan, S. W. Botchway, and V. Kriechbaumer, “Variable-Angle Epifluorescence Microscopy for Single-Particle Tracking in the Plant ER,” *Methods Mol Biol*, vol. 2772, pp. 273–283, 2024, doi: 10.1007/978-1-0716-3710-4_20.

[62] M. von Arx, K. Xhelilaj, P. Schulz, S. zur Oven-Krockhaus, and J. Gronnier, “Photochromic reversion enables long-term tracking of single molecules in living plants.” bioRxiv, p. 2024.04.10.585335, Apr. 12, 2024. doi: 10.1101/2024.04.10.585335.

[63] J. Tang and K. Y. Han, “Extended field-of-view single-molecule imaging by highly inclined swept illumination,” *Optica*, vol. 5, no. 9, p. 1063, Sep. 2018, doi: 10.1364/optica.5.001063.

[64] J. Ren and K. Y. Han, “2.5D Microscopy: Fast, High-Throughput Imaging via Volumetric Projection for Quantitative Subcellular Analysis,” *ACS Photonics*, vol. 8, no. 3, pp. 933–942, 2021, doi: 10.1021/acsphotonics.1c00012.

[65] N. Miura *et al.*, “Adaptive Optics Microscopy with Wavefront Sensing Based on Neighbor Correlation,” *Plant and Cell Physiology*, vol. 64, no. 11, pp. 1372–1382, Nov. 2023, doi: 10.1093/pcp/pcad138.

[66] X. Jin *et al.*, “Membraneless organelles formed by liquid-liquid phase separation increase bacterial fitness,” *Science Advances*, vol. 7, no. 43, p. eabh2929, Oct. 2021, doi: 10.1126/sciadv.abh2929.

[67] A. Schulten *et al.*, “Functional specialization of Arabidopsis VEL polymerization domains in the switch to Polycomb silencing.” bioRxiv, p. 2024.02.15.580496, Feb. 15, 2024. doi: 10.1101/2024.02.15.580496.

[68] J. I. Qüesta, J. Song, N. Geraldo, H. An, and C. Dean, “Arabidopsis transcriptional repressor VAL1 triggers Polycomb silencing at FLC during vernalization,” *Science*, vol. 353, no. 6298, pp. 485–488, 2016, doi: 10.1126/science.aaf7354.

[69] J. D. G. Jones *et al.*, “Effective vectors for transformation, expression of heterologous genes, and assaying transposon excision in transgenic plants,” *Transgenic Research*, vol. 1, no. 6, pp. 285–297, 1992, doi: 10.1007/BF02525170.

[70] M. S. Box, V. Coustham, C. Dean, and J. S. Mylne, “Protocol: A simple phenol-based method for 96-well extraction of high quality RNA from Arabidopsis,” *Plant Methods*, vol. 7, p. 7, 2011, doi: 10.1186/1746-4811-7-7.

[71] J. Schindelin *et al.*, “Fiji: an open-source platform for biological-image analysis,” *Nat Methods*, vol. 9, no. 7, pp. 676–682, Jun. 2012, doi: 10.1038/nmeth.2019.

[72] A. H. Syeda *et al.*, “Single-molecule live cell imaging of Rep reveals the dynamic interplay between an accessory replicative helicase and the replisome,” *Nucleic Acids Research*, vol. 47, no. 12, pp. 6287–6298, Apr. 2019, doi: 10.1093/nar/gkz298.

[73] A. L. Payne-Dwyer, A. H. Syeda, J. W. Shepherd, L. Frame, and M. C. Leake, “RecA and RecB: probing complexes of DNA repair proteins with mitomycin C in live Escherichia coli with single-molecule sensitivity,” *Journal of The Royal Society Interface*, vol. 19, no. 193, p. 20220437, Aug. 2022, doi: 10.1098/rsif.2022.0437.

[74] M. Schwertner, M. J. Booth, and T. Wilson, “Simple optimization procedure for objective lens correction collar setting,” *J Microsc*, vol. 217, no. Pt 3, pp. 184–187, Mar. 2005, doi: 10.1111/j.1365-2818.2005.01431.x.

[75] J. W. Shepherd, A. L. Payne-Dwyer, J.-E. Lee, A. Syeda, and M. C. Leake, “Combining single-molecule super-resolved localization microscopy with fluorescence polarization imaging to study cellular processes,” *JPhys Photonics*, vol. 3, no. 3, 2021, doi: 10.1088/2515-7647/ac015d.

[76] P. Hunter, A. L. Payne-Dwyer, M. Shaw, N. Signoret, and M. C. Leake, “Single-molecule and super-resolved imaging deciphers membrane behavior of onco-immunogenic CCR5,” *iScience*, vol. 25, no. 12, p. 105675, Dec. 2022, doi: 10.1016/j.isci.2022.105675.

[77] G. Grossmann, M. Krebs, A. Maizel, Y. Stahl, J. E. M. Vermeer, and T. Ott, “Green light for quantitative live-cell imaging in plants,” *Journal of Cell Science*, vol. 131, no. 2, p. jcs209270, 2018, doi: 10.1242/jcs.209270.

[78] L. Dresser *et al.*, “Amyloid-β oligomerization monitored by single-molecule stepwise photobleaching,” *Methods*, vol. 193, pp. 80–95, 2021, doi: 10.1016/j.ymeth.2020.06.007.

[79] R. E. Thompson, D. R. Larson, and W. W. Webb, “Precise nanometer localization analysis for individual fluorescent probes,” *Biophysical Journal*, vol. 82, no. 5, pp. 2775–83, 2002, doi: 10.1016/S0006-3495(02)75618-X.

[80] H. Miller, Z. Zhou, A. J. M. Wollman, and M. C. Leake, “Superresolution imaging of single DNA molecules using stochastic photoblinking of minor groove and intercalating dyes,” *Methods*, vol. 88, pp. 81–88, 2015, doi: 10.1016/j.ymeth.2015.01.010.

[81] A. Robson, K. Burrage, and M. C. Leake, “Inferring diffusion in single live cells at the single-molecule level,” *Philosophical Transactions of the Royal Society B: Biological Sciences*, vol. 368, no. 1611, p. 20120029, 2013, doi: 10.1098/rstb.2012.0029.

[82] S. H. Chung and R. A. Kennedy, “Forward-backward non-linear filtering technique for extracting small biological signals from noise,” *Journal of Neuroscience Methods*, vol. 40, no. 1, pp. 71–86, 1991, doi: 10.1016/0165-0270(91)90118-J.

[83] A. Meschichi and S. Rosa, “Visualizing and Measuring Single Locus Dynamics in Arabidopsis thaliana,” in *Arabidopsis Protocols: Methods in Molecular Biology*, vol. 2200, 2021, pp. 213–224. doi: 10.1007/978-1-0716-0880-7_10.

[84] A. J. M. Wollman *et al.*, “Critical roles for EGFR and EGFR-HER2 clusters in EGF binding of SW620 human carcinoma cells,” *Journal of The Royal Society Interface*, vol. 19, no. 190, p. 20220088, 2022, doi: 10.1098/rsif.2022.0088.

[85] A. Payne-Dwyer *et al.*, “Predicting Rubisco:Linker Condensation from Titration in the Dilute Phase.” Physical Review Letters (in press), Feb. 06, 2024. doi: 10.48550/arXiv.2301.05681.

Acknowledgements

We would like to thank Ibrahim Cissé and Jamie Hobbs for preliminary discussions, Pan Zhu, Cecilia Lövkvist, Anna Schulten, Govind Menon, Martin Howard, Grant Calder and Aisha Syeda for training and discussions, Mathias Nielsen and Yaoxi Li for generating the VRN5-mScarlet-I and VIN3-SYFP2 constructs, and the BioScience Technology and Horticulture Facilities at the University of York for supporting confocal microscopy and growth chamber resources. Funded by EPSRC (grants EP/T00214X/1 and EP/T002166/1). For the purpose of open access, a Creative Commons Attribution (CC BY) licence is applied to any Author Accepted Manuscript version arising from this submission.

Author Contributions

Conceptualization, Funding acquisition, administration, supervision; ML, CD. Methodology, software and validation: APD, ML; Investigation, data curation, analysis and visualization: APD, GJJ; Writing – original draft preparation: APD; Writing – review & editing: APD, GJJ, CD, ML.

Competing interests

The authors declare no competing interests.

Supplementary Information

Supplementary Table 1. Primers used in this study

Primer name	**Primer sequence 5' -> 3'**
Primers for cloning	
Mega-pENTR VIN3-mTurq2 F	GCGGCAGCTTCAGCCGTGAGCAAGGGCGAGGAG
Mega-pENTR VIN3-mTurq2 R	GAGTTAATAAATAGACCGATTTCAAAAGCTTTTACTTGTAC AGCTCGTCCATG
VRN5_mScarlet_T	GCATCCGCGGCAGCTTCAGCCGTGAGCAAGGGCGAGGCA
VRN5_mScarlet_B	GTTGAATCAATGGGAAGCTTGATTACTTGTACAGCTCGTCC ATG
qRT-PCR primers	
FP-qPCR-F2	GGACGACGGCAACTACAAGA
FP-qPCR-R2	GTTGCCGTCCTCCTTGAAG
VIN3-qPCR-1F	TGCTTGTGGATCGTCTTGTCA
VIN3-qPCR-1R	TTCTCCAGCATCCGAGCAAG
VRN5_qPCR_F	GAGGCATTGTTAGTAGGCTTCC
VRN5_qPCR_R	CACGCAGCTGGAACTAAATCTC
FLC spliced F	AGCCAAGAAGACCGAACTCA
FLC spliced R	TTTGTCCAGCAGGTGACATC
UBC_qPCR_F	CTGCGACTCAGGGAATCTTCTAA
UBC_qPCR_R	TTGTGCCATTGAATTGAACCC
PP2A F2	ACTGCATCTAAAGACAGAGTTCC
PP2A R2	CCAAGCATGGCCGTATCATGT

Supplementary Table 2. Sample statistics used for quantitative SlimVar analysis. Numbers of nuclei and tracks quantified**.** Col*FRI* acquisitions were aggregated over all tested vernalization conditions (at least 9 cells per condition per growth cycle).

Line	Vernalization / imaging condition	Independent growth cycles	Cells quantified	Nuclear tracks detected
VIN3-SYFP2	NV	3	28	0
	V2W	4	71	1158
	V6W	3	49	933
	V6W T7	3	27	0
VIN3-GFP	NV	3	33	0
	V2W	4	64	994
	V6W	4	83	1485
	V6W T7	4	37	0
VRN5-EYFP	NV	4	54	1122
	V2W	3	36	964
	V6W	4	69	1865
	V6W T14	4	49	1285
VRN5-mScarletI	NV	5	44	552
	V2W	6	29	426
	V6W	2	16	256
	V6W T14	3	29	365
*FLC-lacO/*LacI-YFP	NV	3	27	225
VRN5-mScarletI × *FLC-lacO/*LacI-YFP	NV	3	10	365 × 23
	V2W	2	28	1703 × 156
	V6W	3	25	2867 × 192
	V6W T14	2	18	1416 × 74
Col*FRI*	All (green / 488 nm)	3	80	0
	All (yellow / 514 nm)	3	64	0
	All (red / 561 nm)	3	80	0

Supplementary Table 3. Average stoichiometry of VIN3-SYFP2 whose diffusivity resembles that of a typical *FLC* locus, corrected for endogeneous VIN3.

Line	**Timepoint**	***FLC*-like tracks** $D \approx D_{FLC}$		**Stoichiometry** (molecules)	
		Number	% of total (±sem)	Median	IQR
VIN3-SYFP2	V2W	131	11.3 (1.0)	3.2	2.0–6.0
				6.4	3.9–11.9 *corrected*
	V6W	148	16.5 (1.4)	5.2	3.8–8.4
				10.4	7.6–16.8 *corrected*

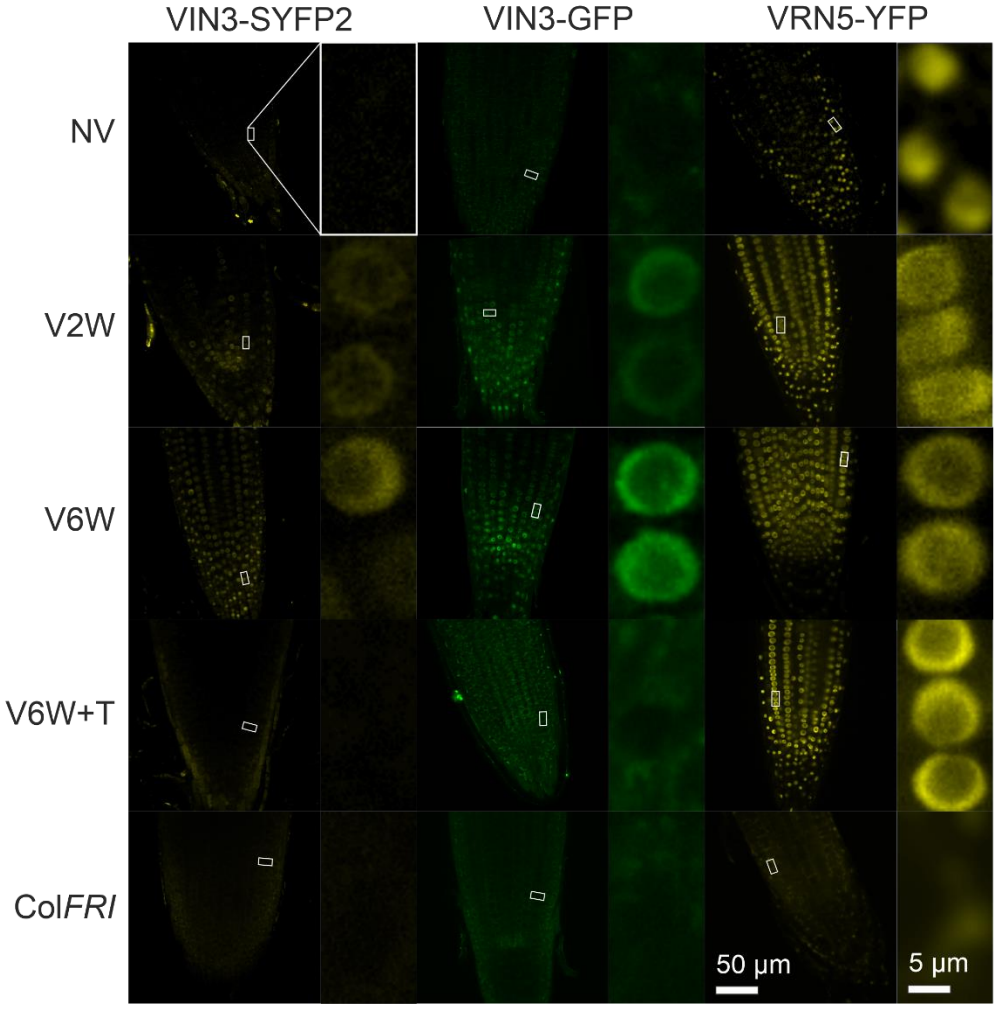

Supplementary Figure 1. Confocal microscopy indicates VIN3 and VRN5 expression increase due to vernalization.

Confocal projections of live whole root tips of VIN3-GFP and VRN5-YFP at different timepoints. NV is non-vernalized; V2W and V6W refers to 2 or 6 weeks of cold respectively; the post-vernalized timepoint V6W+T refers to 7 days warm (V6W+T7) for VIN3 and 14 days warm (V6W+T14) for VRN5. Bright particles outside the root envelope are remnants of the root cap. Also shown are insets at 13× scale to show detail of the labelled protein signals, which are consistently localized to the nucleoplasm, but not the nucleolus of each cell.

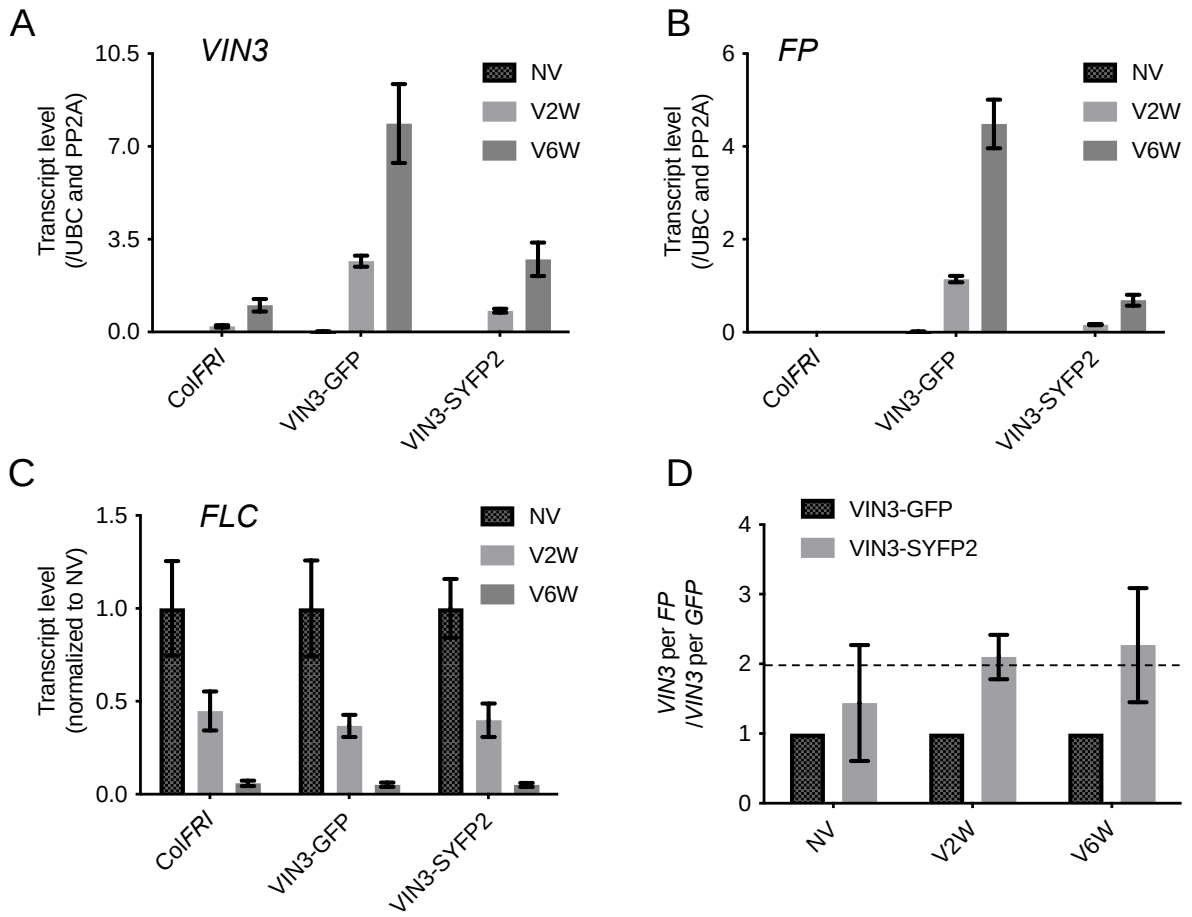

Supplementary Figure 2. RNA expression analysis and characterization of VIN3-SYFP2.

Expression level of *VIN3* (A), fluorescent protein (B) in VIN3-GFP, VIN3-SYFP2 and Col*FRI* seedlings. (C) Expression level of spliced *FLC* in seedlings after 2 weeks and 6 weeks vernalized cold seedlings relative to non-vernalized seedlings. (A-C) Data are presented as mean ± sem (N=9) from three biologically independent experiments. (D) Based on the assumption that protein levels scale proportionally with RNA levels, we derive a correction factor to infer the total number of VIN3 proteins in the yellow line from the detected number of VIN3-SYFP2 proteins. This factor can be estimated by taking the ratio of mRNA expression levels of *VIN3* to *SYFP2*, then normalising this by the ratio of *VIN3* to *GFP* expression in the green line, which lacks endogenous *VIN3*. The error in the correction factor is propagated directly from the sem of the independent measurements in panels A-B. Given the uniform rate of increase of VIN3 expression in all lines regardless of labelling, the correction factor is expected to be constant over time. Taking an inverse-variance-weighted average over the three timepoints, the correction factor used in this work is 2.0 ± 0.7, which is consistent with the expected genotype of the yellow line: a single exogenous gene copy of *VIN3-SYFP2* and a single native gene copy of *VIN3*.

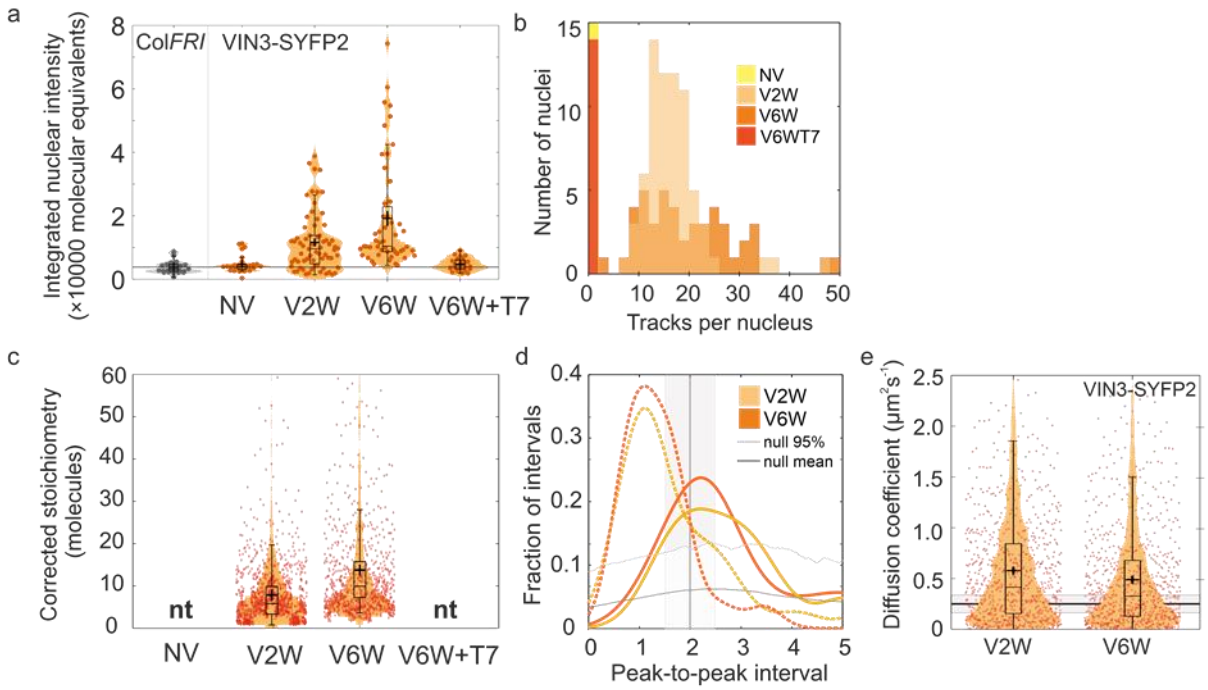
a
Integrated nuclear intensity (×10000 molecular equivalents)
ColFRI VIN3-SYFP2
NV V2W V6W V6W+T7
b
Number of nuclei
Tracks per nucleus
NV
V2W
V6W
V6WT7
c
Corrected stoichiometry (molecules)
nt
nt
NV V2W V6W V6W+T7
d
Fraction of intervals
Peak-to-peak interval
V2W
V6W
null 95%
null mean
e
Diffusion coefficient (μm²s⁻¹)
VIN3-SYFP2
V2W V6W

Supplementary Figure 3. Collated SlimVar observations of VIN3-SYFP2. a) Distributions of integrated nuclear intensity of VIN3-SYFP2 in individual nuclei before, during and after vernalization. In the VIN3-SYFP2 line, the unlabelled, endogenous fraction of VIN3 protein can be accounted for by a factor of 2.0 ± 0.7 derived from the relative mRNA expression levels (Supplementary Fig. 2). Bar, box and whisker denote median, interquartile range (IQR) and 1.5× IQR respectively; cross: mean ± sem. Nuclear protein copy numbers of VIN3-SYFP2 range from negligible before cold (410 ± 560 molecules, BM test vs. Col*FRI*, N=52, p= 0.52 |ns), through 7,800 ± 1,600 molecules above background at 2 weeks cold (N=68, p<0.001|**) up to a peak of 15,000 ± 3,000 molecules at 6 weeks cold (N=51, p=0.0045|*). At 7 days after transfer to warm, the number of VIN3-SYFP2 again drops to a negligible amount (900 ± 700 molecules per nucleus, BM test vs. Col*FRI*, N=54, p=0.08|ns). b) The mean number of VIN3 tracks per nucleus cannot be distinguished between VIN3-SYFP2 and VIN3-GFP, nor does this change significantly between 2 and 6 weeks' vernalization in either case (V2W: 16.3 ± 1.0 and 18.3 ± 1.9, N=120, p=0.42|ns; V6W: 17.4 ± 2.4 and 17.9 ± 1.8, N=140, p=0.22|ns respectively). c) After accounting for unlabelled VIN3, the mean labelled stoichiometry increases from 7.8 ± 2.7 molecules at 2 weeks' cold to 13.8 ± 3.9 at 6 weeks' cold (N=1792 tracks, p<0.001). d) The stoichiometry distribution for VIN3-SYFP2 has a smaller periodicity (dashed lines), which is incompatible with an integer number of molecules greater than one. However, after accounting for unlabelled VIN3, the resulting periodicity (2.2 ± 0.8, V2W; 2.2 ± 0.8, V6W, solid lines) is also consistent with dimeric subunits in VIN3 assemblies during vernalization.

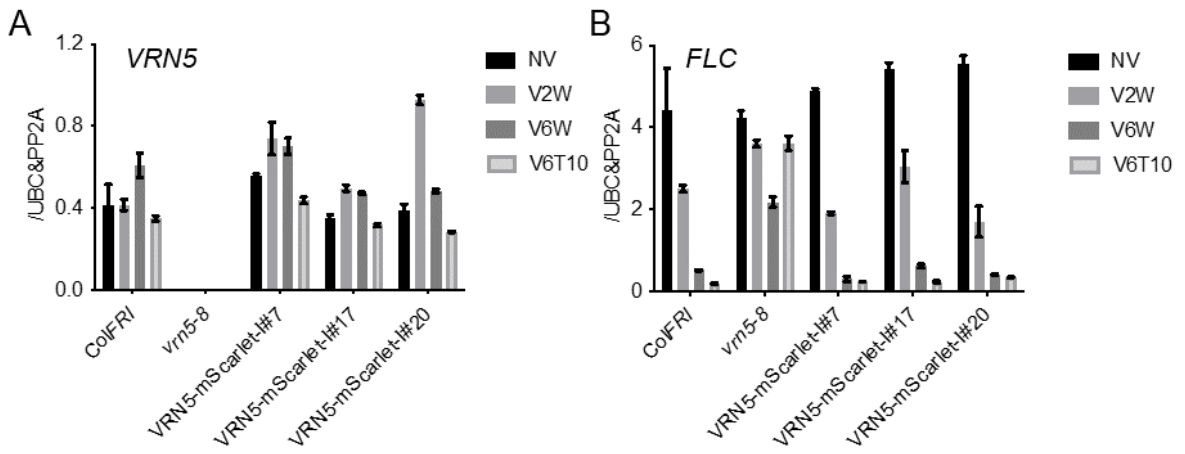

Supplementary Figure 4. RNA expression analysis of *VRN5* and *FLC* in single-colour VRN5-mScarlet-I lines. Expression level of *VRN5* (A), of spliced *FLC* (B) in VRN5-mScarlet-I, *vrn5-8* and Col*FRI* seedlings before (NV) and after 2 weeks and 6 weeks cold treatments (V2W, V6W). V6T10 represents 10 days after a 6 week-cold treatment. Data are presented as mean ± SD (N=3) from 1 biological experiment. The samples of VRN5-mScarlet-I are from heterozygous T2 seedlings.

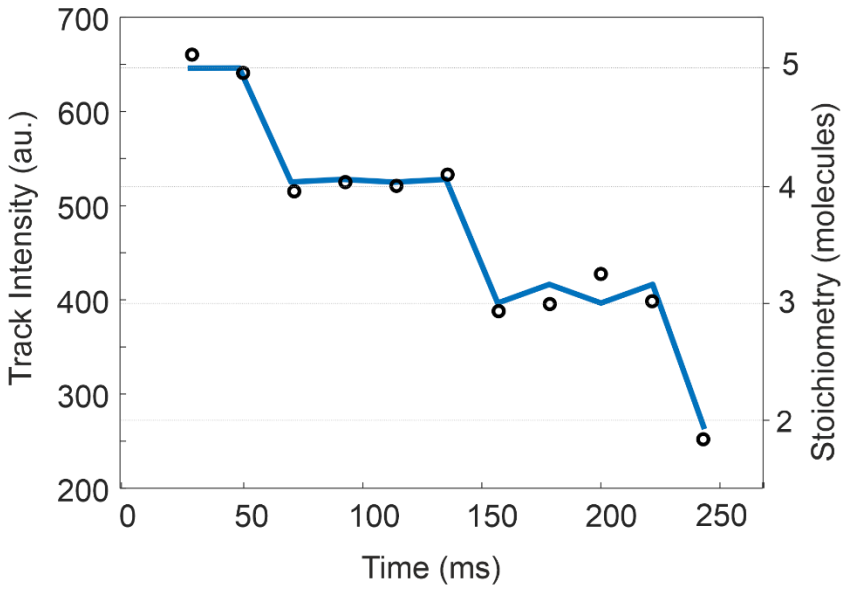

Supplementary Figure 5. Determination of characteristic single molecule brightness in live tissues. Intensity of foci near the end of a single track in a VRN5-YFP image sequence (black circles), interpolated using a Chung-Kennedy edge-preserving filter (centred window of 3 points, blue line). The consistent photobleaching steps yield an estimate of about 126 counts for the characteristic single-molecule brightness of the VRN5-YFP fusion *in planta*. Normalization of the intensity trace by this value gives the absolute number of active fluorophore reporters over the entire course of photobleaching.

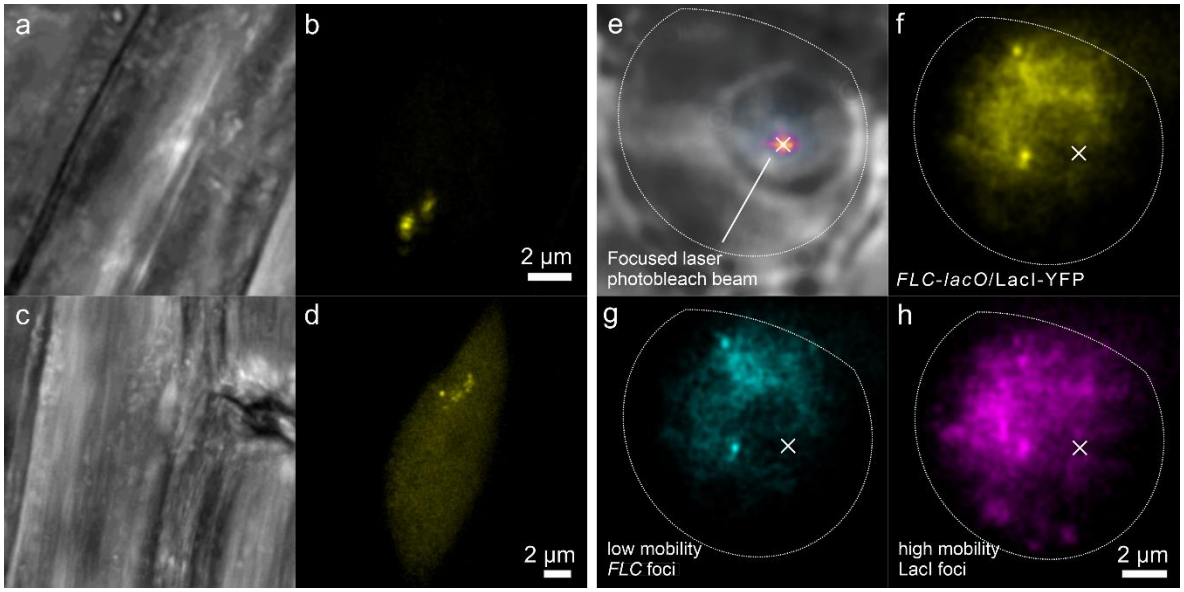

Supplementary Figure 6. Confocal and SlimVar imaging of the FLC-*lacO*/LacI-YFP line. a-d) Confocal: a) Transmission and b) confocal fluorescence imaging of a nucleus in the epidermal meristem showing at least 2 loci, and c,d) a nucleus in the epidermal elongation zone, featuring additional pairs of *FLC* foci consistent with endoreduplication. Mobile LacI-YFP form a uniform background due to motion blur. Scale bars 2 µm. e-h) SlimVar: e) a large nucleus (dotted outline) of a cortical cell imaged in brightfield with superposed intensity profile of a focused laser beam (cross) inside the nucleolus; an initial exposure with this beam, typically 30 s, removes excess unbound LacI-YFP that diffuses through the excitation volume, while preserving any bound to the *lacO* array at the *FLC* transgene; f-h) the subsequent SlimVar acquisition shown as f) mean average, g) median projection showing isolated and low mobility *FLC* foci at the expected frequency of ≥2 loci per nucleus, whose diffusivity is quantified and used to match the diffusivity of VIN3 and VRN5 proteins of interest under the same acquisition conditions (Table 1); and h) standard deviation projection indicating residual fast-moving LacI-YFP. In spot-bleached nuclei, we find a mean of 4.4 ± 0.8 slow LacI-YFP tracks per nucleus (N=38 nuclei) reflecting the expected two *FLC* transgenes plus a minority of endoreduplication loci. At the observed particle number density, the likelihood of random overlap of more than two free LacI-YFP tetramers is extremely low. We therefore identify all LacI-YFP tracks with stoichiometry greater than three tetramers, or a threshold of 12 LacI-YFP, as potential *FLC* loci. These tracks exhibit a diffusion coefficient (Fig 4a) of D_{FLC} = 0.20 ± 0.02 $\mu m^2 s^{-1}$ (N=129, mean ± sem, 20 ms exposure). Tracks in the upper quartile of LacI-YFP stoichiometry (>81 LacI-YFP molecules), corresponding to the brightest foci per nucleus, yield an equivalent diffusivity estimate of 0.17 ± 0.04 $\mu m^2 s^{-1}$ (N=36; p= 0.097 |ns). With or without pre-bleaching, tracks with fewer than 12 LacI-YFP molecules typically diffuse faster, around 0.54 ± 0.04 $\mu m^2 s^{-1}$ (N=153; p= 0.0094 |*), which suggests they may consist of free LacI tetramers.

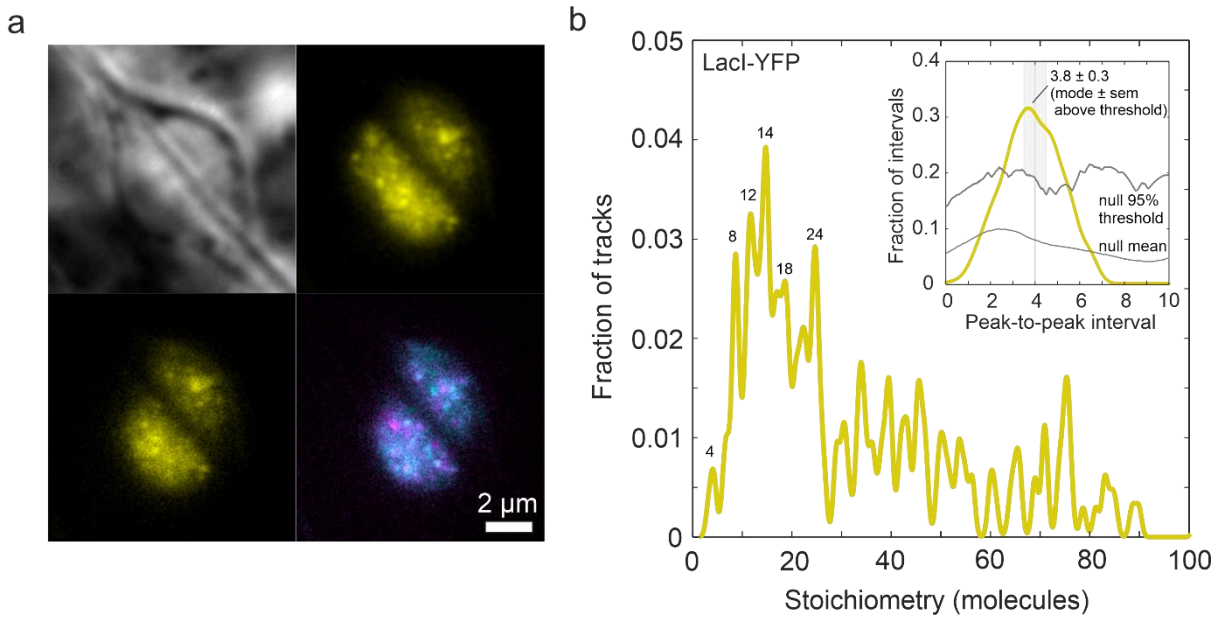

Supplementary Figure 7. Tetrameric spacing of LacI-YFP validates peak interval extraction from stoichiometry distributions. a) Representative SlimVar images of neighbouring nuclei before vernalization in single-colour *FLC-lacO*/LacI-YFP line, shown as brightfield, initial SlimVar frame, and projections of mean (yellow), and merged median (cyan) and standard deviation (magenta) respectively over 5 frames immediately following pre-bleaching. b) The stoichiometry of detected LacI-YFP tracks (n=225) shows clear peaks at approximate multiples of 4, with occasional interceding multiples of 2, consistent with the tightly bound tetrameric (dimer-of-dimer) complex of LacI. The maximum stoichiometry observed is 380 molecules (not shown for clarity). Inset: the most common spacing between neighbouring peaks in the stoichiometry distribution as estimated by the new method. The threshold above which the null distribution can be rejected is the 95th percentile fraction of intervals (grey trace) output from simulated random stoichiometry (Methods). The most common interval is given by the modal peak value above the null threshold (3.8 ± 0.3 molecules), which is consistent only with integer 4 molecules, and thus a tetrameric repeat unit as expected.

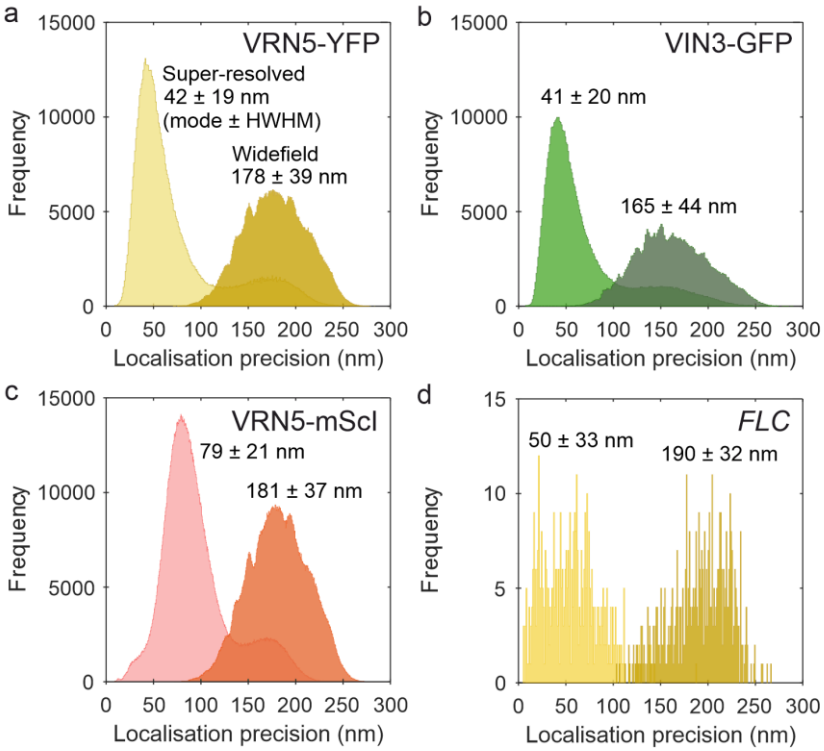

Supplementary Figure 8. Localization precision of tracked fluorescent foci in SlimVar acquisitions. Super-resolved localization precision [79] and Gaussian-fit widefield FWHM of foci within a) VRN5-YFP tracks (n= 5326), b) VIN3-GFP tracks (n=2479) at 2 ms exposure per frame; c) VRN5-mScI tracks (n=6395) and d) *FLC-lacO*/LacI-YFP loci (n=475) at 20 ms exposure.

Supplementary Video legends

Supplementary Video 1. SlimVar dynamic assemblies of VRN5-YFP in live root tips.

A single nuclear acquisition of VRN5-YFP line at non vernalized conditions showing distinct assemblies. Left: raw data; right: photobleach corrected and Gaussian smoothed by 1 pixel width to emphasise dynamic assemblies. Scale bar: 1 µm, frame duration 2 ms, frame rate 25 fps.

Supplementary Video 2. SlimVar resolves dynamic assemblies of VIN3-GFP in live root tips.

A representative SlimVar acquisition in VIN3-GFP line at 2 weeks' cold. Scaling and framerate as in Video 1. VIN3 has significantly lower copy number and stoichiometry compared to VRN5, and background is higher in GFP channel relative to YFP.